UNIVERSITÄT AUGSBURG
Universitätsbibliothek

OPEN ACCESS
OPUS AUGSBURG

The upgraded ASDEX Upgrade contribution to the ITPA confinement database: description and analysis

F. Ryter, C. Angioni, G. Tardini, Gregor Birkenmeier, P. David, M. Dunne, R. Fischer, T. Pütterich, J. Schweinzer, J. Stober

Angaben zur Veröffentlichung / Publication details:

Ryter, F., C. Angioni, G. Tardini, Gregor Birkenmeier, P. David, M. Dunne, R. Fischer, T. Pütterich, J. Schweinzer, and J. Stober. 2021. "The upgraded ASDEX Upgrade contribution to the ITPA confinement database: description and analysis." *Nuclear Fusion* 61(4): 046030. https://doi.org/10.1088/1741-4326/abe4b0.

Nutzungsbedingungen / Terms of use:

CC BY 3.0

Dieses Dokument wird unter folgenden Bedingungen zur Verfügung gestellt: / This document is made available under these conditions:
CC-BY 3.0: Creative Commons - Namensnennung
Weitere Informationen finden Sie unter: / For more information see:
https://creativecommons.org/licenses/by/3.0/de/deed.de

nuclear fusion
IAEA

PAPER • OPEN ACCESS

The upgraded ASDEX Upgrade contribution to the ITPA confinement database: description and analysis

To cite this article: F. Ryter *et al* 2021 *Nucl. Fusion* **61** 046030

View the article online for updates and enhancements.

You may also like

- The updated ITPA global H-mode confinement database: description and analysis
G. Verdoolaege, S.M. Kaye, C. Angioni et al.
- Energy and particle confinement in JET H-mode plasma
M. Maslov, A. Boboc, M. Brix et al.
- Recent progress on the development and analysis of the ITPA global H-mode confinement database
D.C. McDonald, J.G. Cordey, K. Thomsen et al.

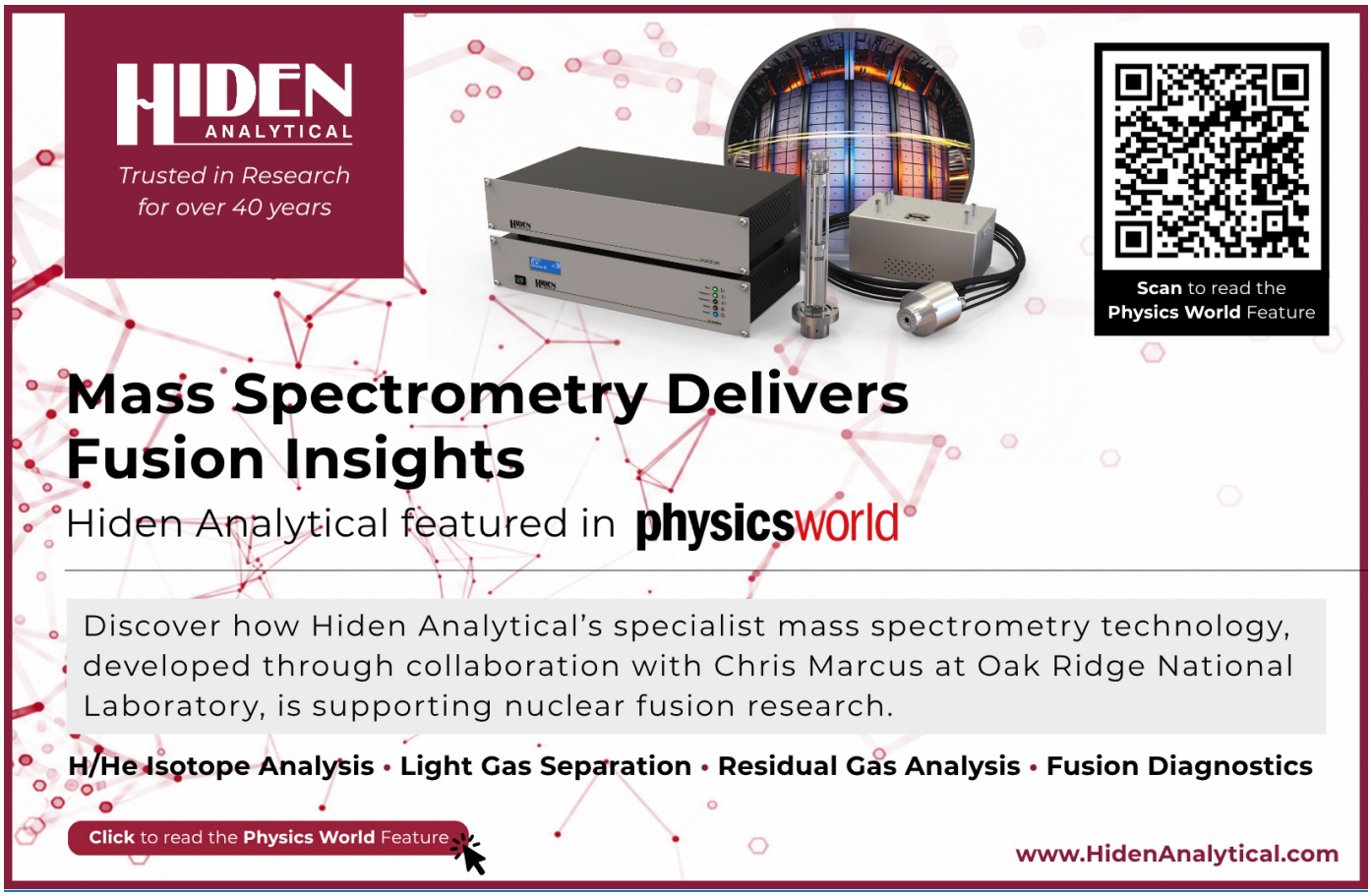

This content was downloaded from IP address 137.250.102.76 on 05/11/2026 at 09:21

OPEN ACCESS
IOP Publishing | Bureau International des poids et Mesures Nuclear Fusion
Nucl. Fusion **61** (2021) 046030 (32pp) https://doi.org/10.1088/1741-4326/abe4b0

The upgraded ASDEX Upgrade contribution to the ITPA confinement database: description and analysis

F. Ryter*, C. Angioni, G. Tardini, G. Birkenmeier, P. David, M. Dunne, R. Fischer, T. Pütterich, J. Schweinzer, J. Stober, The ASDEX Upgrade Team[a] and The EUROfusion MST1 Team[b]

Max-Planck-Institut für Plasmaphysik Garching, Germany

E-mail: ryter@ipp.mpg.de

Received 20 November 2020, revised 15 January 2021
Accepted for publication 9 February 2021
Published 17 March 2021



Abstract

The ITPA multi-machine confinement database has been recently extended, in particular to account for the effect of the metallic plasma facing components installed in the ASDEX Upgrade and JET tokamaks during the last decade. Confinement data from the ASDEX Upgrade tokamak have been contributed to the ITPA confinement database since 1994. The present version, which includes data from 1994 to 2017, is described and discussed in this article. The aim of this work is to document the database before it is made public and report on the main results on the confinement properties reflected in this database. Through the transition from carbon to metallic wall, the operation at low density originally accessible with the carbon wall, has been strongly limited by the occurrence of tungsten accumulation. However, at medium and high densities, the confinement properties with the carbon and metallic walls are rather similar. The database analysis yields in both cases a rather strong plasma current dependence and a clearly negative magnetic field dependence. The density dependence is negligible, while the well-known positive impact of triangularity appears very clearly. These dependences are partly at variance with the widely-used IPB98(y,2) confinement scaling, but in agreement with the analysis of the upgraded ITPA multi-machine and JET databases. The confinement degradation observed at high density with strong gas puffing can be clearly attributed to the density profile in the outer plasma region, as reported in previous studies.

Keywords: H-mode confinement, confinement database, density behaviour, energy confinement time

(Some figures may appear in colour only in the online journal)

1. Introduction

The confinement properties of H-mode plasmas in tokamaks are generally characterised in comparison with the IPB98(y,2) confinement scaling developed by the International Tokamak Physics Activity topical group on transport and confinement and published in the ITER Physics Basis [1]. This expression was obtained by analysing the multi-machine confinement database version DB3, containing data from discharges performed until 1996. Following this work, the database has been extended, yielding DB3v13 in 2007, described and discussed in [2], but IPB98(y,2) remained the reference for confinement comparisons and predictions. More information on the various versions of the ITPA database can be found in [3]. As tokamak operation has evolved since that time, the ITPA

* Author to whom any correspondence should be addressed.
[a] See Meyer *et al* 2019 (https://doi.org/10.1088/1741-4326/ab18b8) for the ASDEX Upgrade Team.
[b] See Labit *et al* 2019 (https://doi.org/10.1088/1741-4326/ab2211) for the EUROfusion MST1 Team.

Original content from this work may be used under the terms of the Creative Commons Attribution 3.0 licence. Any further distribution of this work must maintain attribution to the author(s) and the title of the work, journal citation and DOI.

Coordinating Committee recommended to extend the ITPA confinement database and eventually provide a new scaling taking into account the latest results and knowledge. This seemed particularly important because of the change of the plasma facing components from carbon to metal in the ASDEX Upgrade and JET tokamaks and the database had to account for this change.

The multi-machine analysis based on version DB5v2.3 (completed in the year 2020) is described and discussed in [3]. In this work new scaling law expressions are given, in particular ITPA20-IL which applies to tokamaks with metallic walls and to which the results presented in the present paper are compared in section 5. Compared to DB3v13 from 2007, the database has been mainly extended with recent data from the ASDEX Upgrade (AUG) and JET tokamaks. The JET contribution is presented and discussed in [4]. In the present work we describe the contribution from the ASDEX Upgrade tokamak to the ITPA DB5v2.3 confinement database and discuss its main confinement properties.

The AUG device started operation in 1991 such that its contribution to DB3 was limited to 102 discharges in a rather narrow operation range, in particular in plasma current, heating power and at low triangularity. This initial dataset had been extended for DB3v13 which contained 643 AUG time points from discharges run until June 2002. Further data from AUG have been added to DB3v13, in particular contributing with hybrid discharges to the work reported in [5] and building DB4v5. The number of AUG entries in DB4v5 was then 1590 from discharges performed until February 2006. The version presented here includes the DB4v5 dataset extended for the new contribution to the ITPA database and for the present work with discharges performed between 2007 and 2017.

Since 2007 the plasma facing material in AUG is tungsten, building the 'W-wall' in contrast to the previous 'C-wall' made out of graphite. In the transition from the carbon to the so-called tungsten wall, the surface of the tungsten plasma facing components was increased in steps, started end of 1999 with 3% of the surface and reaching 100% for the 2007 experimental campaign with shot 21 482. Details can be found in [6–9]. We labelled the period starting with this discharge as 'W-wall'. This also corresponds to the clear and significant reduction of the H-mode power threshold reported in [10]. This change in power threshold is attributed to a steeper edge density profile in the L-mode preceding the L–H transition [11], through a deeper penetration of the neutrals with the metallic wall compared to the carbon one [12].

We emphasise that we present here some results on the properties of the confinement time in ASDEX Upgrade as they can be deduced from the database, but that this article is by far not an overview of all the confinement studies carried out in this device.

The public access to this version of the AUG confinement database occurs through the ITPA and EUROfusion organisations.

The paper is structured as follows. The next section provides general information on the AUG tokamak and a description of the dataset. It is followed by section 3 which deals with the behaviour of the electron density and its relation with the particle source. In section 4 the main confinement properties are discussed in comparison to the IPB98(y,2) confinement time scaling to make the link with previous results. In sections 5 and 6 properties of the energy confinement time as yielded by the dataset are analysed and discussed in detail. The last section consists of a summary and conclusions.

2. Description of the AUG contribution

2.1. Generalities

The AUG dataset contributed to the DB5v3.2 version of the ITPA database [3], contains 2411 time slices. The version described here consists of DB5v3.2 extended with 620 data points to populate more the extremes of the plasma current range: $I_p \leqslant 0.6$ MA and $I_p \geqslant 1.1$ MA. The aim of this addition was to better assess the I_p and B_T dependences. As discussed in the next section, the rather strong positive I_p and the clear negative B_T dependences reported in [3] are confirmed by the additional data.

The database includes data from discharges performed in a period of time from June 1994 to October 2017, shot number 4670 to 34 962. More recent discharges are not included yet to respect the scientific property of the original physics proposals. The total number of the data points is 3031, gained from 1599 plasma discharges. From these discharges, 1402 were run until the end of 2013 and therefore under the IPP-EURATOM collaboration. The 197 plasmas included in the dataset run since 2014 were performed within the framework of the EUROfusion Consortium, either under the MST1 programme (128), or in the internal AUG programme (69).

The major and minor radii of AUG are respectively 1.65 m and 0.5 m, while the plasma elongation is around 1.6 and varies little for the data of the present database. The device is equipped with three heating methods: neutral beam injection (NBI), ion cyclotron heating (ICRH) and electron cyclotron heating (ECRH). The reader can find an overview of the heating systems in [13]. The NBI system is provided by eight beams delivering 2.5 MW each for 10 s for deuterium injection, yielding a maximum power of 20 MW. The modification of the system in which the geometry of two beams has been re-oriented to be more tangential for current drive purposes is described in [14]. The NBI is the main heating power for H-mode confinement studies and the maximum power in the database is 17 MW. In addition, the ICRH system yields up to 8 MW for 10 s through four generators, providing central heating at 2 or 2.5 T at frequencies of 30 MHz or 36.5 MHz respectively. In the deuterium plasmas included in the database the heating scheme is hydrogen minority. This heating method has been used on AUG since its start [13]. The ECRH has been first been installed in 1996 with the system ECRH-I which delivered up to 2 MW for 2 s with four beam-lines when it was completed [15]. This system has been extended with the installation of ECRH-II which delivers up to 4 MW for 10 s through four additional beam-lines and went gradually into operation from 2005 on [16, 17]. Thus, high power long pulse ECRH was available and widely used since the completion of the W-wall. The system is mostly running at 140 GHz in the second

harmonic X-mode scheme which corresponds to central deposition at 2.5 T and 100% electron heating. Recently ECRH-I has been replaced by ECRH-III which delivers 4 MW with four beam-lines such that, together with ECRH-II, the total ECRH power amounts to 8 MW. Data from discharges with ECRH-III have not been included in the database yet as these are very recent. The ECRH and ICRH are often applied in combination with NBI.

Between 1991 and 1996, AUG was run with an open divertor, named Div-I, replaced in 1996 by Div-II, a closed divertor with increased pumping capability thanks to a cryo-pump [18]. There have been different versions for Div-II labelled a, b, c and d and finally Div-III in use since 2014 [19]. The Div-II and Div-III divertor versions all have the same basic geometry and similar pumping properties, they differ only in the details of the exact shape or target plate material [18–20].

As indicated above, the surface of the plasma facing components was initially made out of graphite (C-wall) and replaced gradually by tungsten to build the 'full tungsten wall' (W-wall) in 2007. Therefore, in the following we will distinguish the C-wall and W-wall periods in some of the analyses.

The large majority of the discharges consists of ELMy H-modes, with only very few exceptions such as ELM-free H-modes and L-modes at very high density included for comparisons. The repartition of the H-modes in different ELM types is discussed in subsection 5.9.

As shown in the next sub-section, the dataset presented here covers a wide range in control parameters such as plasma current (I_p) magnetic field (B_T), safety factor (q_{95}), heating power, as well as line-averaged density ($\bar{n}_e$) and Greenwald fraction $f_{GW} = \bar{n}_e/n_{GW}$where $n_{GW} = 10I_p/(\pi a^2)$ with a being the minor radius and units 10^{19} m^{-3}, MA and m. For simplicity, in the following the line-averaged density is labelled n_e instead of $\bar{n}_e$. These data are obtained from the usual diagnostics and analysis methods.

For the heating powers the actual deposited power of the different heating methods is used: for NBI all the fast ion losses are subtracted while for the wave heatings the absorption in the plasma is taken into account, generally 80% for ICRH and 100% for ECRH. The total heating heating power, P_{heat}, is then the sum of these heating powers and also includes the Ohmic power. For the confinement analyses we use, as for the ITPA scalings, the thermal confinement time $\tau_{th} = W_{th}/P_{loss}$, named TAUTH in the ITPA database, where W_{th} is the thermal plasma energy, which does not contain the fast ion contribution, while $P_{loss} = P_{heat} - dW_{th}/dt$ is the usual 'thermal loss power', labelled PLTH in the ITPA database. The estimate of W_{th} requires the calculation of the NBI losses and fast ion content (W_{fi}) which is subtracted from the total plasma energy W_{tot}. In AUG W_{tot} is very close to W_{mhd} deduced from the equilibrium [21] which is therefore generally used as W_{tot}. The values of W_{fi} were so far calculated by a formula using global plasma parameters. However, in comparison with TRANSP calculations, it has been recently noticed that there was a trend to underestimate W_{fi}. This has been corrected in the present version of the database by either using the TRANSP values when available otherwise using a fit to them. These revised W_{fi} data are about 50% higher than the previous one which

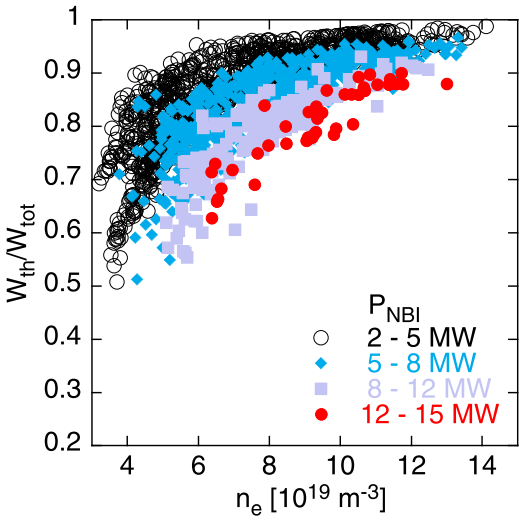

Figure 1. Ratio W_{th}/W_{tot} versus density for different ranges of NBI power.

therefore yields somewhat lower values of τ_{th} in the low density range in the present database compared to the previous versions. This correction has also been included in the data contributed to version DB5v3.2 of the multi-machine ITPA confinement database. It has a negligible impact on the result of the multi-machine regressions. The new calculation of the fast ion contribution to plasma energy and its impact on the confinement values is described in more details in a companion paper [21], including a new method based on the RABBIT code [22]. Figure 1 shows the ratio W_{th}/W_{tot} versus density to illustrate the contribution of the fast ions to plasma energy for different levels of NBI heating power. At low density the contribution of W_{fi} to total plasma energy can reach up to 50% but this contribution decreases strongly as density is increased. As expected it also depends on the NBI power.

As usual in database confinement analyses, in our work too the power radiated by the main plasma (P_{rad}) is not subtracted from the heating power in the calculation of the confinement time. Cases with high radiation, defined as $P_{rad}/P_{lth} \geqslant 0.6$, are excluded from the standard analysis of the ITPA multi-machine database, see [3, 23]. In AUG, such cases are rare for discharges performed with the C-wall. With the W-wall, at low density, strong central accumulation of tungsten generally often happens limiting the operational space [8, 9, 24]. This happens in particular in discharges aiming at high confinement time, e.g. at high plasma current and/or rather low heating power. In such cases the central radiation caused by tungsten increases with time leading to a strong decrease of the effective central heating power, loss of confinement, transition to L-mode and disruption. In addition such phases are not stationary and inadequate for confinement studies. As a consequence, in the W-wall at low density there are practically no discharges with good confinement as shown below (e.g. figure 26). Adding central ECRH helps avoiding tungsten accumulation but simultaneously tends to degrade confinement, as discussed in section 5. It is underlined that the lack of data from low density H-modes with the W-wall is not

due to the fact that these discharges have not been included in the database but mainly because of operational reasons. Note that this is also the case for JET-ILW. Independently of the cases with tungsten accumulation, it should however be underlined that there is a trend in the present AUG database for the averaged value of P_{rad}/P_{loss} to be about 5% higher with the W-wall compared to the C-wall, with a trend to be lower towards high density. However, due to the very different radiation profiles of the impurities C and W, the latter being more central, this comparison does not provide reliable information on the possible impact on the confinement time estimate. On the other side, a dedicated analysis of the radiated power measured by the bolometer cameras for about 100 H-mode discharges in the W-wall reveals that the power radiated inside the surface $\rho_{pol} = 0.98$ relative to the heating power ranges between 10% and 30% with a rather flat distribution. For the same discharges, an estimate of the power radiated by tungsten based on the measurement of the tungsten concentration indicates that the radiation losses due to tungsten in the plasma core are below 10% of the heating power for most of the cases, a few points only reaching 20%. As the discharges included in the database have central heating, the radiation power density in the central part of the plasma is much smaller than that of the heating power density there, such that the impact of the radiated power in the W-wall on confinement time remains small. A deeper quantitative estimate of this effect on the whole database, which requires profile analysis, is out of the scope of this work.

The data included in the database are averaged over the respective time intervals, whose length is at least 100 ms, which roughly corresponds to one confinement time, up to several seconds when the plasma is in steady state. In general the time interval length corresponds to several confinement times. The time intervals are chosen such that the quantities such as plasma current, magnetic field, plasma shape, heating power, plasma energy, radiated power are constant. The electron density is in general also constant with the exception of density ramps during which, however, the relative change of the density during the respective time interval is lower than 10% for the very large majority of the entries. There is no discrimination on the presence of sawteeth but cases with neoclassical tearing modes (NTM) are generally not included in the database. There are however a few points with NTM to allow for a comparison with the MHD-free points. The entries with NTM are identified in the variable phase and are excluded from the analyses.

As already shown two decades ago in [25, 26] and confirmed in the next sections the edge electron density at the separatrix and in the scrape-off layer (SOL) impacts on confinement. This quantity is provided by the lithium beam diagnostic [27]. We used here the SOL density ($n_{e,SOL}$) which is defined here as the density in the SOL averaged over the radial region $1.01 < \rho_{pol} < 1.03$ in the equatorial plane, ρ_{pol} being the usual normalised poloidal flux radius. This corresponds to a geometrical distance of about 3 cm in the outer mid-plan. Taking the data further outside might be influenced by the proximity of the limiters of the ICRH antennas in some cases. We prefer to use here $n_{e,SOL}$ instead of the separatrix density ($n_{e,SEP}$), at $\rho_{pol} = 1.0$, because the latter is subject to a larger scatter as the uncertainties on the separatrix position can have a strong impact on $n_{e,SEP}$ due to the steep density gradient of the pedestal. The values of $n_{e,SEP}$ are however also included in the dataset. Overall $n_{e,SEP}$ is somewhat higher than $n_{e,SOL}$ but roughly proportional to it. The difference is larger at low values of $n_{e,SOL}$ than at high values and it also increases with plasma current. In the same context of analyses we will also use the neutral gas pressure in the divertor (P_{div}) provided by gauges [28].

The main working gas in ASDEX Upgrade is deuterium, but discharges in hydrogen and helium have also been performed and some data points of these discharges have been included in the database. The characteristics of these points are briefly presented in the appendix A. Some points with impurity seeding are also included in the database and discussed in the appendix A as well. These impurities are mainly helium, nitrogen, neon and argon. Helium has been introduced originally in dedicated experiments to investigate helium transport and pumping [29], a crucial issue for ITER. But in addition, until 2008 the AUG vessel has been regularly conditioned with ^{4}He glow discharge such that an undesirable residual concentration up to 10% was always intrinsically present in the plasmas, leading to poorer confinement, as reported in [30]. Such glow discharges have been avoided since 2008 as much as possible, meaning in practice that it has been very rarely used after the completion of the W-wall. In the recent years the detrimental effect of helium on confinement has been further investigated in dedicated discharges with helium seeding [31]. A confinement decrease of about 10% is observed for a helium concentration of about 5%.

The other impurities were introduced for investigations on the reduction of the power loads in the divertor, see e.g. [32, 33]. In particular, nitrogen has been extensively used during the recent years, whereby it has been found that N-seeding induces a confinement improvement through its impact on the pedestal profiles [34–38]. The reader is referred to these publications for more details on the possible effect on confinement.

In the remaining of the paper we focus exclusively on the deuterium discharges, hydrogen and helium plasmas are not included such that no investigation of the mass dependence is performed. For the investigation of these topics in AUG the reader is referred to [39, 40] for hydrogen and [31] for helium.

The next subsection provides information on the content of the database corresponding to this working gas, in particular the ranges covered by the main control plasma parameters.

2.2. Range of the main confinement-relevant control parameters

In a first stage, the ranges of the control parameters which are relevant for confinement are compared in the following plots. The ranges of I_p, B_T and q_{95} are displayed in figures 2(*a*) and (*b*). As it is important to investigate possible confinement differences in the C and W walls we indicate the two time periods in the plots with different symbols. For more clarity in these plots and some of the following ones, the I_p values in MA have been rounded such that the second decimal is 0 or 5, while for

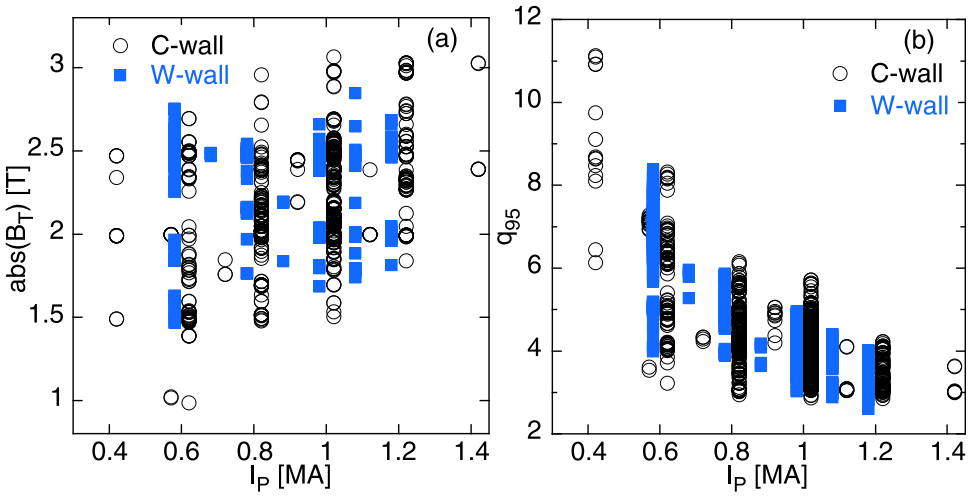

Figure 2. Range covered by plasma current, magnetic field and safety factor for the C and W wall periods. (*a*) Magnetic field versus plasma current. (*b*) Edge safety factor versus plasma current.

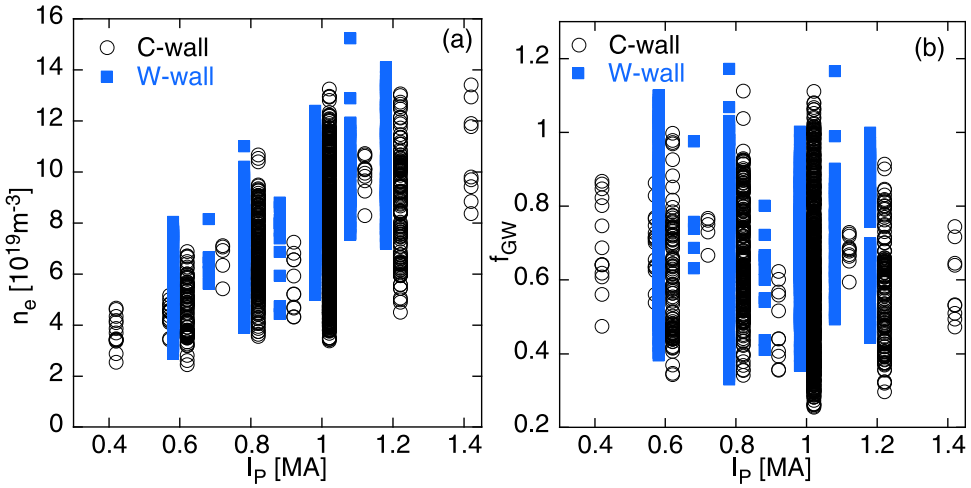

Figure 3. Electron density versus plasma current for the C and W walls: panel (*a*) line average density; panel (*b*) Greenwald fraction.

a better identification of the different categories, here C and W, the I_p value has been in addition artificially shifted by ± 0.02.

The plasma current covers the range 0.4–1.4 MA and 0.6–1.2 MA for C and W respectively, B_T 1–3 T for C and 1.5–2.8 T for W. There are, however, very few plasmas below 0.6 MA and at 1.4 MA. It should be underlined that the NBI fast ions are poorly confined for $I_p < 0.6$ MA, conditions which are not favourable for confinement studies as this causes large uncertainties on the absorbed NBI power. The variations in I_p and B_T lead to a range in edge safety factor q_{95} for each I_p shown in panel (*b*) of figure 2. Even if the ranges in q_{95} covered at each plasma current have different extensions, there is an overlap in the middle range of the q_{95} values. This provides possibilities to investigate possible effects of q_{95}. For the C-wall the lowest value of q_{95} at 0.8 MA is 3 while it goes down to only 4 in the W-wall at this current, requiring $B_T \approx 1.5$ T. Adding lower q_{95} value in the W-wall might be a possible future extension of the dataset.

Density and Greenwald fraction ranges for C and W are displayed in figures 3(*a*) and (*b*) respectively. The line-averaged density has been varied over a very wide range in the C-wall, but, whereas the upper values of n_e in the W-wall are comparable, the lower values are not as low as those for the C-wall for higher plasma currents, which reflects the fact that W accumulation often hampers H-mode operation at low density. Panel (*b*) indicates that correspondingly the Greenwald fraction covers overall a rather wide range and reaches values around 1 for almost all of the I_p values.

A further important quantity is triangularity (δ) which plays a positive role for confinement in H-modes. As done for the ITPA database, δ is the average value of the upper and lower values of triangularity calculated at the separatrix, as yielded by the MHD equilibrium. The values of the lower and upper triangularity are roughly co-linear such that δ is an appropriate quantity to take this effect of the plasma shape into account. Note that δ in the AUG dataset is always positive and can therefore be used in the regressions, while $1 + \delta$ is used in the analysis of the multi-machine database because this quantity is zero for circular plasmas. The windows explored by this quantity in the C and W walls data are shown in figure 4. The range

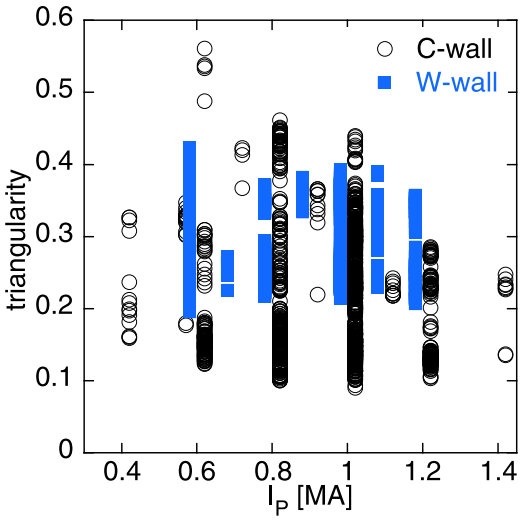

Figure 4. Triangularity versus plasma current for the C and W walls.

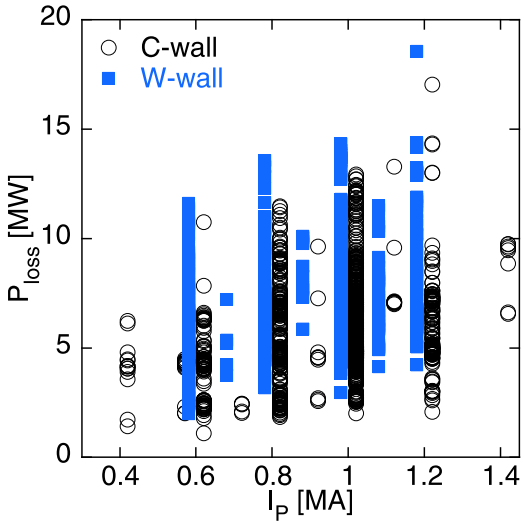

Figure 5. Variation of the heating power versus plasma current with indication of the wall material.

covered by δ during the C-wall period is wider than for the W-wall data by about a factor of two. The upper boundary for C is somewhat higher and values as low as 0.1 are found for almost all the I_p values while for the W-wall the lowest values are about 0.2. This is, at least partly, a result of attempts to keep good confinement at the higher densities for operation with the W-wall. Future extensions to lower values with the W-wall might be useful to better assess the confinement dependences.

In summary, the ranges of the main control parameters in C and W walls are both rather wide, whereby those of the C data cover a somewhat wider region. This reduces the correlations between the quantities, as will be shown in section 5. A further important parameter, heating power, is discussed in the following sub-section.

2.3. Heating power

The majority of the discharges included in the database was heated with NBI only, or NBI combined with ECRH and/or ICRH. There is only a reduced number of cases heated by ECRH and/or ICRH alone. The repartition of the time points for each combination is provided in table 1.

As shown in figure 5, the range in heating power is wide, reaching 12 to 15 MW in many cases, even higher for a few points. This wide range in heating power is important for the assessment of the power dependence of the confinement time which has a strong impact on the predictions for future devices. At low current, in particular 0.4 MA, the maximum power is limited by the low density. In addition, at this I_p value the NBI fast ions are not well confined leading to high losses to the wall.

The relative contributions of ECRH and ICRH to the total auxiliary heating power are indicated by the distribution displayed in figures 6(*a*) and (*b*). The distributions shown here do not include the discharges heated by NBI only (0 on the *x*-axis) and which build the majority of the discharges, see table 1. It

Table 1. List of the number of points for the different heating methods applied to the discharges. The labels are self-explaining: NBI only (NBI), NBI + ECRH (NBEC), NBI + ICRH (NBIC), NBI + ECRH + ICRH (NBECIC), ECRH + ICRH (ECIC).

Method	NBI	NBEC	NBIC	NBECIC	EC	IC	ECIC
No. of points	1700	678	533	70	3	45	2

should be underlined that the present dataset is representative for confinement studies but does not reflect the overall contributions of ECRH and ICRH to the physics studies in AUG. The distribution for ECRH indicates that the contribution of this heating method to the total heating power is generally modest, in general 10% to 20% as discharges with ECRH-III are not included in the present dataset. However, ECRH deposited in the plasma centre, even at low power levels, is often a necessary ingredient to avoid tungsten accumulation as recognised early in the transition from carbon to tungsten [9, 41–44]. The contribution of ICRH is higher reaching more than 30% of the total heating power in many discharges. Heating in the centre with ICRH also contributes to hampering tungsten accumulation [44]. This is reflected by the data: ECRH and/or ICRH have be applied in about 90% of the discharges included in the present database and performed in the W-wall at $f_{GW} \leqslant 0.6$. At higher densities this fraction is about 70%.

For the usual direction of the plasma current in AUG, the only case included in this dataset, the neutral beams are only injected in the co-direction. Therefore, the torque applied by the NBI and the heating power are strongly correlated, with rather modest variations due to the geometry of the various beams. Additional variations are provided by applying ICRH or ECRH, but this is limited by the fact that these powers are often smaller than that of the NBI. There are exceptions for discharges at rather low heating power, in particular some of them had ICRH only for dedicated studies of plasmas with low torque. The relation between torque and heating power is

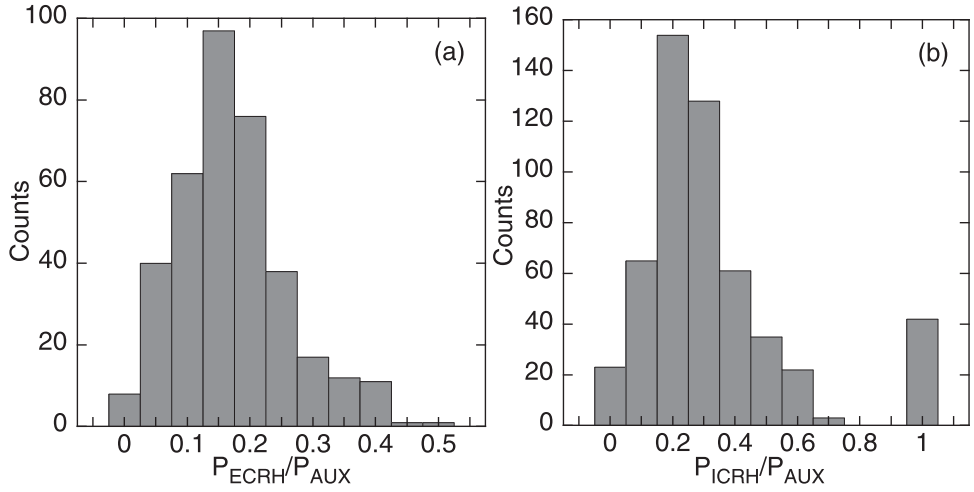

Figure 6. Distribution of the ECRH and ICRH contributions to the heating power, panels (*a*) and (*b*) respectively. In panel (*a*) the three time points with ECRH only have been omitted to provide a more detailed distribution in the interesting range of $P_{\mathrm{ECRH}}/P_{\mathrm{aux}}$.

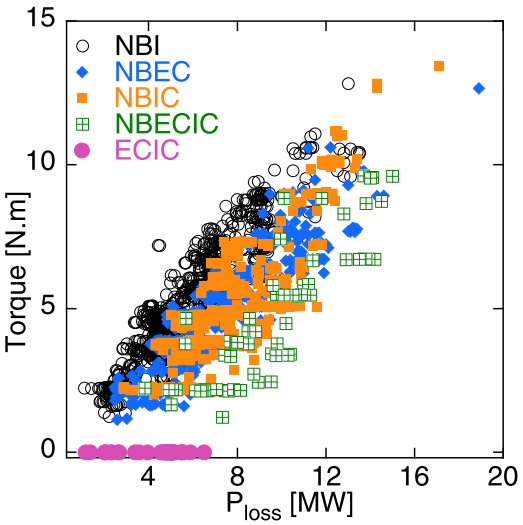

Figure 7. Applied torque by the NBI versus loss power. The symbols indicate the different mixtures of heating methods.

shown in figure 7, which indicates that indeed significant variations of torque could be only achieved at heating powers up to about 5 MW.

2.4. Operation ranges of the different confinement scenarios

During the last three decades, numerous attempts along several lines of operational scenarios were carried out worldwide to further enhance the confinement beyond that of the H-mode and to search for good confinement conditions compatible with low divertor power loads. Such scenarios performed in AUG and included in the database are briefly described below.

In the mid-nineties the so-called 'completely detached high-confinement' scenario (CDH) has been developed in AUG [45]. These plasmas were obtained with adequate neon seeding such that small ELMs of type-III appeared and that the power load in divertor was very low. They had good confinement at densities close to the Greenwald density, with a rather peaked density profile. The heating power was at most 10 MW and due to the high density and radiated power these plasmas were generally just above the H-mode threshold power [46]. The present database includes 29 CDH time points.

Over the last 25 years, so-called advanced scenarios have been developed applying various operational approaches to achieve a higher confinement than in usual H-modes. Such plasmas have also been developed in AUG since 1997 and named 'improved H-modes', see e.g. [34, 47, 48]. For this purpose the widely-used approach has been applied which consists in heating the plasma very early in the current ramp-up to impose a broad current profile [49], such that the most successful improved H-modes had no sawteeth, no NTMs despite high normalised β values (β_{N}). With the C-wall, this method produced plasmas with very low density, leading to very high ion temperatures and excellent confinement with $H_{98(y,2)}$ reaching up to 1.8. These plasmas are characterised by low collisionality, high ion temperature with peaked profiles, $T_{\mathrm{i}} > T_{\mathrm{e}}$ and very high toroidal rotation. Such discharges react very sensitively to some additional gas puffing or ECRH power with a strong decrease of T_{i} and rotation leading to $T_{\mathrm{i}} \approx T_{\mathrm{e}}$ with a significant confinement reduction [50, 51]. The original method for improved H-modes could not be used any longer with the W-wall due to tungsten accumulation and similar scenarios but at higher density and with central ECRH were developed to avoid tungsten accumulation [34, 52–54]. In addition such discharges are now generally performed with a very fresh boronisation. The database contains such plasmas from both the C and W wall periods.

The database also contains points from the so-called ITER baseline (ITER BL) discharges, see [55, 56] for AUG. These are run at values of some dimensionless parameters which are close to those foreseen for ITER: $\beta_{\mathrm{N}} \approx 1.8$, $q_{95} \approx 3$, $f_{\mathrm{GW}} \approx 0.8$. In addition the triangularity is around 0.4 which is close to the highest value which can be reached in AUG. Such plasmas are also included in the database. A multi-machine database dedicated to the study of ITER baseline scenarios has been compiled by the ITPA topical topical group on integrated

operational scenarios presented and discussed in [57] which the reader is referred to for more details on this topic.

In the ITPA confinement database the advanced scenario discharges, e.g. improved H-modes for AUG, are labelled with the qualifier 'HYBRID' which we also applied to the database presented here. In the present dataset, the label HYBRID is only based on the fact that heating power was applied early in the current ramp-up and is therefore only an operational label. A physics criterion based, for instance, on the shape of the current profile cannot be used for such a database with a very large number of entries. It should be underlined that applying early heating is, by far, not a guarantee for high confinement, such that a number of the points with the best confinement are labelled HYBRID, but the confinement of many HYBRID points is not particularly high, as will be shown in section 4.3. A study of the role of the current profile and of applying 'early heating' or 'late heating' has been discussed in [49]. In the following plots we differentiate between the HYBRIDs performed during the C-wall and W-wall periods labelled respectively HYBRID-C and HYBRID-W. There are less HYBRID-W points than HYBRID-C but they are representative.

The ITER BL points are clearly identified by the parameters indicated above and in practice this means for AUG: high plasma current, low magnetic field, rather low power, high triangularity and most of them with the W-wall.

The overview of the data included in the database for these scenarios is given in the following figures which show how the usual ELMy H-mode, HYBRID, ITER BL and CDH points are distributed in the operational space of some of the control parameters. Starting with heating power and triangularity: figure 8 shows that, as mentioned above, the ITER BL points are grouped in a limited range in heating power. Figure 9 indicates that they are indeed concentrated in the higher range of triangularity. The HYBRID-C discharges cover a large range in heating power and a rather wide range in triangularity while the HYBRID-Ws cover narrower ranges. The CDH points, which are only at 1 MA, are in the moderate power range and with quite low triangularity.

Turning to density, both n_e and f_{GW}, figure 10 shows that the ITER BL are limited to the high density range which we will discuss later. The HYBRID-C entries cover a wide range in density, in particular for $I_p = 1$ MA, with many points at low density, clearly below the W points for the reasons indicated above. The CDH points reach f_{GW} close to unity. The ELMy H-modes cover the largest operational window.

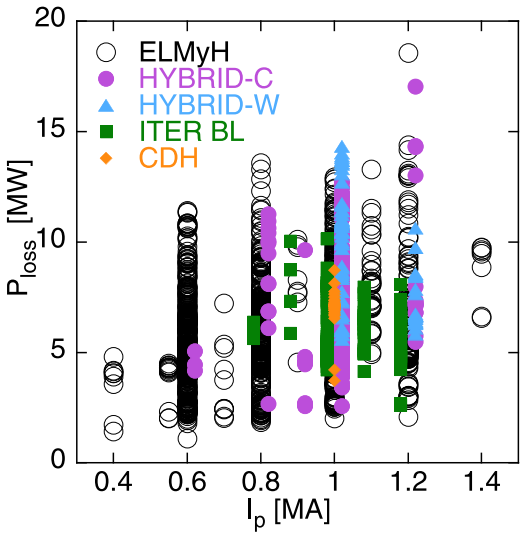

Figure 8. Heating power versus plasma current with different symbols for the different scenarios explained in the text.

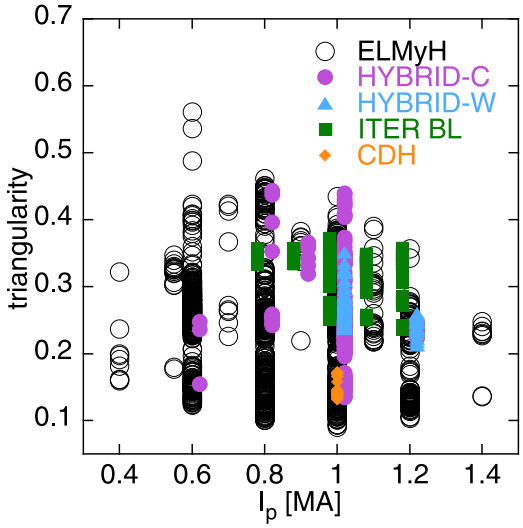

Figure 9. Triangularity versus plasma current with different symbols for the different scenarios explained in the text.

3. Particle source and electron density

In this section the features induced by the open and closed divertor geometries on neutral retention and SOL density are presented. The behaviour and dependences of the line-averaged electron density are presented and discussed.

3.1. Divertor types, neutral gas and edge density

As mentioned above, the first divertor in AUG, Div-I, had an open geometrical configuration, whereas the following divertors Div-II and Div-III were closed [18–20, 58].

This is illustrated in figure 11 for the Div-I and the Div-IIa versions showing clearly the differences in geometry. Note for Div-II the cryo-pump, at liquid helium temperature, which is installed on the low field and pumps below the outer baffle of the divertor. This pumps is also present in Div-III. The open and closed configurations impact on the neutral gas retention in the divertor which is higher for a closed configuration. This affects the ratio between the neutral gas pressure in the divertor (P_{div}) and in the main chamber, the so-called compression ratio, and consequently the relationship between P_{div} and density in the SOL and at the edge of the plasma: for a given neutral gas density in the divertor region, the density in the SOL is lower for the closed divertor compared to the open one. This is clearly reflected by the data shown in figure 12. It should be underlined that turning off the cryo-pump does not

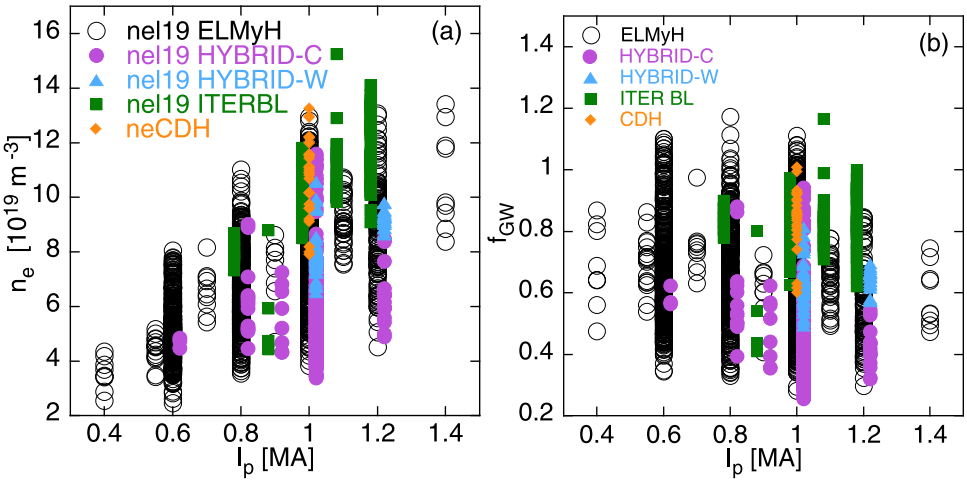

Figure 10. Density versus plasma current with different symbols for the different scenarios explained in the text. Plot (*a*) line-averaged density. Plot (*b*) Greenwald fraction.

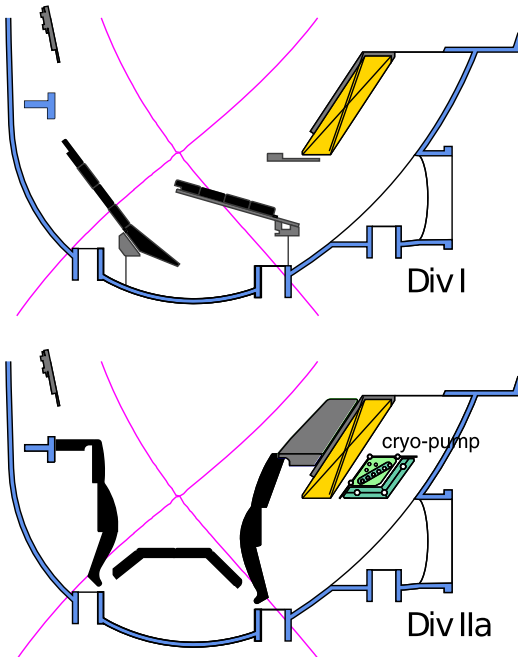

Figure 11. Geometries of the open Div-I divertor and of the closed Div-IIa divertor with cryo-pump.

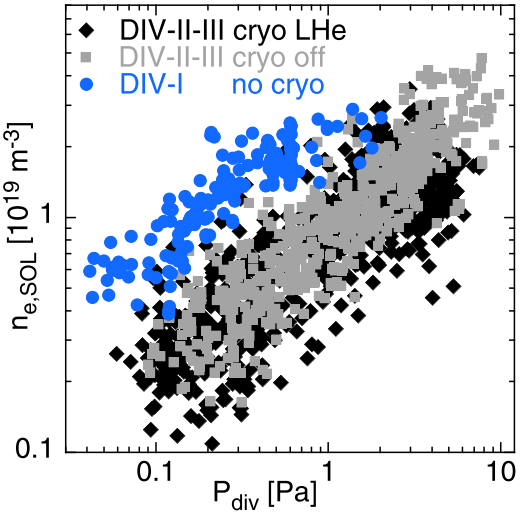

Figure 12. SOL density versus neutral gas pressure in the divertor for Div-I (open geometry) and Div-II and Div-III (closed geometries). Meaning of the symbols: 'cryo LHe' pumping by cryo-pump at helium temperature, 'cryo off' cryo-pump turned off or at liquid nitrogen temperature.

change the relation between P_{div} and $n_{e,SOL}$. The cryo-pump has been, in particular, turned off to reach very high P_{div} and $n_{e,SOL}$ values which cannot be achieved with the maximum available gas puffing flux when the cryo-pump is on. This has been used in particular for the results presented in [33, 59–61]. Figure 12 shows that indeed the highest P_{div} and $n_{e,SOL}$, upper right corner of the plot, could be reached when the cryo-pump was turned off.

3.2. Behaviour of the core electron density

It is well-known that the electron density in the H-mode increases with plasma current and triangularity through the impact on the pedestal stability which leads in general to large ELMs at rather low frequency, see e.g. [25, 62]. Further increase is generally achieved with gas and/or pellet fuelling. Particle transport in the plasma core also plays a role see e.g. [63] and references therein. In this section we investigate the behaviour of the electron density as yielded by our database.

Following the analysis of the dependences of the density reported in [25] for a combined analysis in AUG and JET and recently in [4] for JET, we made regressions using the present database to investigate the dependences in AUG and compare them to these previous results. The main dependences are plasma current, magnetic field, heating power, triangularity and particle source. The particle source is provided by gas puffing through the valves, wall recycling, both at the edge, and in addition by NBI in the core. Discharges with pellet fuelling are not included in this dataset. In AUG, the value of the NBI fuelling is on average about 1.5×10^{20} particles per second for

Table 2. Results of the regressions for the density and Greenwald fraction for the C and W walls. The units are 10^{19} m^{-3}, MA, T, MW.

Label	ζ	α_{I_p}	α_{B_T}	α_δ	$\alpha_{n_{e,SOL}}$	$\alpha_{P_{loss}}$	RMSE
n_e-C	22.4	1.070	−0.542	0.242	0.302	−0.116	0.141
n_e-W	16.9	0.858	−0.455	0.274	0.197	−0.003	0.113
f_{GW}-C	2.49	0.104	−0.540	0.366	0.326	−0.190	0.152
f_{GW}-W	1.67	−0.064	−0.409	0.341	0.244	−0.070	0.116

one MW of NBI. This source in the plasma core only plays a role at low density (low edge source) because it is at least one order of magnitude smaller than the highest gas fuelling (up to 8×10^{22} s^{-1}) applied in the high density cases. In such a global database the NBI central particle source is difficult to take into account quantitatively in conjunction with the edge sources, gas puffing and recycling. Therefore, following [25], we use here $n_{e,SOL}$ as rough approximation to characterise the particle source. The divertor neutral pressure could also be used and yields similar results but $n_{e,SOL}$ is preferred here because the relation between the particle source in the main plasma and P_{div} depends on the divertor geometry. In addition $n_{e,SOL}$ also reflects the recycling which is not necessarily the case for P_{div}. Note that the gas puffing rate through the valves is not adequate because, in AUG, it is very often not representative of the actual situation due to the long reaction time of the plasma to the injection of gas through the valves such that steady-state is often not reached. In addition it does not reflect the recycling contribution.

The regressions are performed according to the usual power law model as least square fit on logarithmic scale and the scaling expression is then of the form:

$$n_e = \zeta I_p^{\alpha_{I_p}} B_T^{\alpha_{B_T}} P_{loss}^{\alpha_{P_{loss}}} \delta^{\alpha_\delta} n_{e,SOL}^{\alpha_{n_{e,SOL}}} \quad (1)$$

where ζ is the numerical factor and α_x the exponents of the regressors. The results of the regressions for density and Greenwald fraction are given in table 2 for the C and W datasets separately.

We start with the first two rows giving the dependences for n_e. As known for a long time and also reflected here, in the H-mode the dependence of density on plasma current is close to linear. The negative dependence on B_T might be due to its impact on the pedestal stability and ELM frequency which play a key role in the global particle confinement. Indeed, as reported in [36, 37], the pedestal stability improves with increasing β, (lower B_T) and the ELM frequency is generally observed to decrease with decreasing B_T. The triangularity δ also plays a significant positive role, however the exponents found here are smaller than the value of about 0.6 reported in [25]. The exponents for $n_{e,SOL}$ are clearly smaller than unity which reflects a saturation of the density increase with gas puffing which is in agreement with the 'fuelling limit' described in [60]. Note that the saturation is stronger for the W-wall as $\alpha_{n_{e,SOL}}$ is smaller. Finally, the dependence on heating power is negative but very weak. In fact, one would expect a stronger negative effect of P_{loss} caused by the increase of particle transport and by the increase of the ELM frequency with heating power. These two effects might be partly compensated by the NBI particle fuelling which is not taken into account here. With the aim of testing very roughly a possible impact of the NBI particle source, we added to $n_{e,SOL}$ a term proportional to NBI power such that it has only a significant impact at low density. For this purpose we set this contribution such that for 10 MW of NBI power the value 0.5×10^{19} m^{-3} is added to $n_{e,SOL}$. Under this assumption, the regressions yields $\alpha_{P_{loss}} \approx -0.3$ and a somewhat stronger impact of the edge source on n_e which is the expected trend.

The respective dependences for the C and W datasets are rather similar but for the W data the numerical factor and $\alpha_{n_{e,SOL}}$ are smaller which leads to smaller values of n_e for given values of the other parameters as will be illustrated below.

The exponents for the density regressions are roughly comparable to those obtained for JET [4]. In particular, in JET also the value of the exponent for the particle source is smaller for the metallic wall than for the carbon wall. In this analysis of the JET data the triangularity is taken into account through $1 + \delta$ and not δ. Using $1 + \delta$ as regressor for the AUG data (not shown in table 2) yields exponents of 1.42 and 1.19 for C and W respectively, the other exponents remaining almost unchanged. These values for $\alpha_{1+\delta}$ are smaller than those found for JET which are between 2 and 2.6.

The comparison of the above expressions with the data is shown in figure 13 in which n_e is plotted versus the corresponding expressions of table 2 n_e-C or n_e-W. This graph exhibits a rather good agreement between the data and the fits. The density is somewhat underestimated by n_e-C for some CDH discharges which is probably due the rather high neon concentration and the observed density peaking. The ITER BL shots reach the highest densities due to the high plasma current, high triangularity and low heating power and some of these points are underestimated by n_e-W.

The Greenwald fraction, f_{GW}, is a widely used and meaningful normalisation of density. The results of the regressions for this quantity are provided in rows 3 and 4 of table 2. As expected from the normalisation by n_{GW} which is proportional to I_p, α_{I_p} is small but the other exponents are very similar to those of n_e.

This behaviour is illustrated in figure 14 which shows the curves for the expressions f_{GW}-C and f_{GW}-W of table 2 versus $n_{e,SOL}$ for three representative values of δ and for standard values in AUG, $I_p = 1$ MA, $B_T = 2.5$ T and $P_{loss} = 10$ MW. These curves indicate clearly how f_{GW} increases with δ and how for a given value of δ the increase of f_{GW} with $n_{e,SOL}$ exhibits a trend to saturate. This saturation is somewhat more pronounced for the W-wall than for the C-wall indicating that higher edge particle source is required with the W-wall to reach a given value of f_{GW}, as also been underlined in [61]. Setting B_T to 2 T instead of 2.5 T induces for both the C and W curves

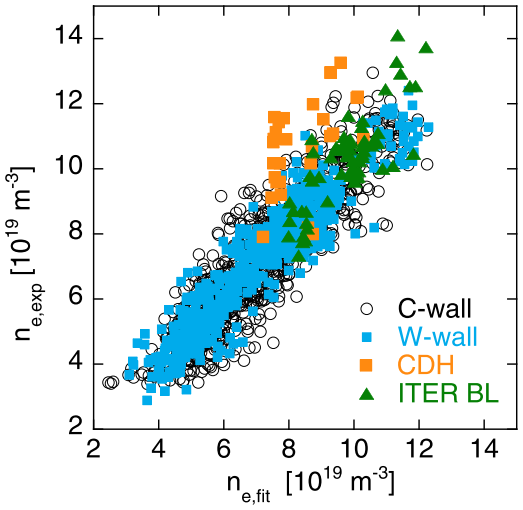

Figure 13. Comparison of the electron density to the values predicted by expressions n_e-C and n_e-W.

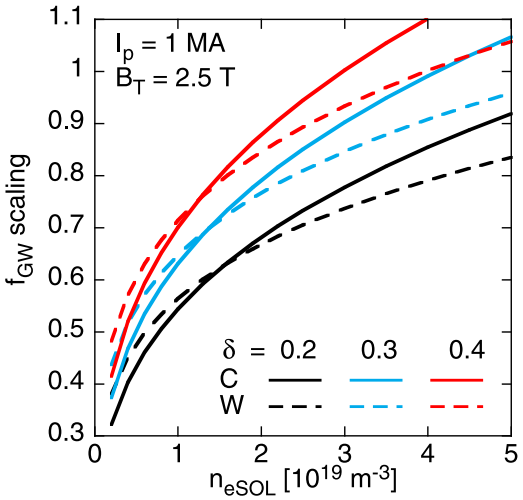

Figure 14. f_{GW} versus $n_{e,SOL}$ calculated with the expressions f_{GW}-C and f_{GW}-W from table 2 for different values of δ and $I_p = 1$ MA, $B_T = 2.5$ T and $P_{loss} = 10$ MW.

a vertical shift of about 10% for the higher values of $n_{e,SOL}$ (not shown).

The dependences of f_{GW} on $n_{e,SOL}$ and δ yielded directly by the data are visualised in figure 15 which shows contour plots for f_{GW} for the C and W data, panels (a) and (b) respectively. Based on the regressions, the range in B_T has been limited to $1.7\ \text{T} \leqslant B_T \leqslant 2.7\ \text{T}$ to create clearer patterns. The scale for δ is identical for the two plots to allow for a quantitative comparison of the contours. We remind here that the range in δ for the W-wall data is narrower than for those of the C-wall, see figure 4, explaining the lack of low δ values for the W data. The two contour plots reflect the properties expressed by the regressions and by figure 14. They both exhibit the fact that, neglecting the rather weak dependences on B_T and P_{loss}, for a given value of $n_{e,SOL}$ a somewhat higher value of δ is required in the W-wall compared the C-wall to reach the same value of f_{GW}. Or conversely for a given value of δ a higher value of $n_{e,SOL}$ is necessary in the W-wall to reach the same value of f_{GW} as in the C-wall.

The high density region in the high field side SOL, the so-called HFSHD, see [64] for more details, is more pronounced in the W-wall. This leads to a stronger outwards shift of the pedestal density profile with respect to the temperature profile which has a negative impact on pedestal stability and therefore confinement time [36], also found in other devices [38] and references therein. This difference between C and W walls is in agreement with the observation reported in [36] from experiments carried out in the W-wall showing that nitrogen seeding reduces the HFSHD and the outwards shift of the pedestal density profile. This improves the stability of the pedestal and therefore confinement. The gas puffing can be reduced such that $n_{e,SOL}$ decreases while n_e and f_{GW} remain constant or might even slightly increase. One may speculate that nitrogen plays in the W-wall the role of the intrinsic carbon concentration in the C-wall which naturally limited the magnitude of the density outwards shift.

It must be underlined that the scaling expressions presented in here are not valid in the presence of light impurity seeding. This is demonstrated in [36] figure 7 for nitrogen seeding which exhibits a very clear decrease of $n_{e,sep}$ with the increasing impurity concentration while the density remains almost constant. Such a behaviour is also yielded by the database for $n_{e,SOL}$. The effect of this mechanism on confinement will be discussed in section 5.7.

As mentioned above, in the analyses of the L–H transition, it has been shown that in the L-mode before the L–H transition the penetration of the neutrals is deeper with the W-wall than with the C-wall leading to a more effective fuelling [12] and one would have expected a lower and not a higher $n_{e,SOL}$ value in the W-wall. However, in the H-mode, this effect seems to be too weak to dominate, which is attributed to two effects which screen the neutral penetration. Firstly, in the studies of the effect of the neutral penetration for the L–H transition [12], $n_{e,SOL}$ was around $0.5 \times 10^{19}\ \text{m}^{-3}$ which is at the lowest boundary of the values in the present confinement dataset. Secondly, in the H-mode the density gradient of the pedestal is much steeper than in the L-mode conditions before the L–H transition which also strongly reduces the neutral penetration.

Another essential aspect must be underlined: the dependences of f_{GW} on I_p and P_{loss} being very weak, the $n_{e,SOL}$ value required to reach a given value of f_{GW} depends mainly on δ and B_T. This means that for given values of δ and B_T the absolute value of $n_{e,SOL}$ determines f_{GW} and not $n_{e,SOL}/n_{GW}$ which would strongly depend on I_p.

This is illustrated in figure 16 for a selection of W data in the narrow ranges $0.8 \leqslant f_{GW} \leqslant 0.9$ and $0.28 \leqslant \delta \leqslant 0.35$, windows which roughly correspond to values envisaged for ITER. Choosing these ranges results in $1.7\ \text{T} \leqslant B_T \leqslant 2.6\ \text{T}$ and $5\ \text{MW} \leqslant P_{loss} \leqslant 10\ \text{MW}$ but in a wide range in I_p. Despite the large scatter, the data in figure 16(a) clearly indicate a quite weak decrease ($I_p^{-0.24}$) of $n_{e,SOL}$ for the selected values of f_{GW} and δ. In contrast, the same data plotted for $n_{e,SOL}/n_{GW}$ in panel (b) indicate a strong decrease ($I_p^{-1.14}$). This suggests that even if the value of n_e corresponding to a given value of f_{GW}

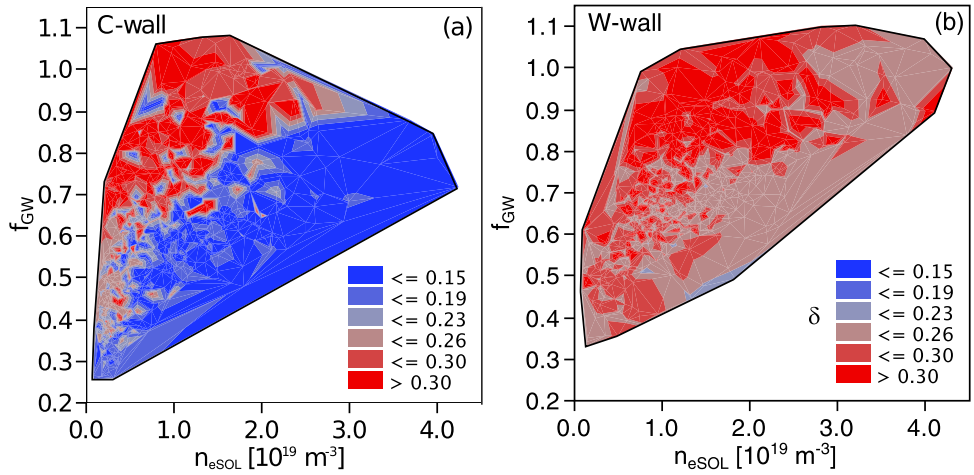

Figure 15. Contour plots of f_{GW} versus $n_{e,SOL}$ for values of δ: panel (*a*) for the C-wall, panel (*b*) for the W-wall.

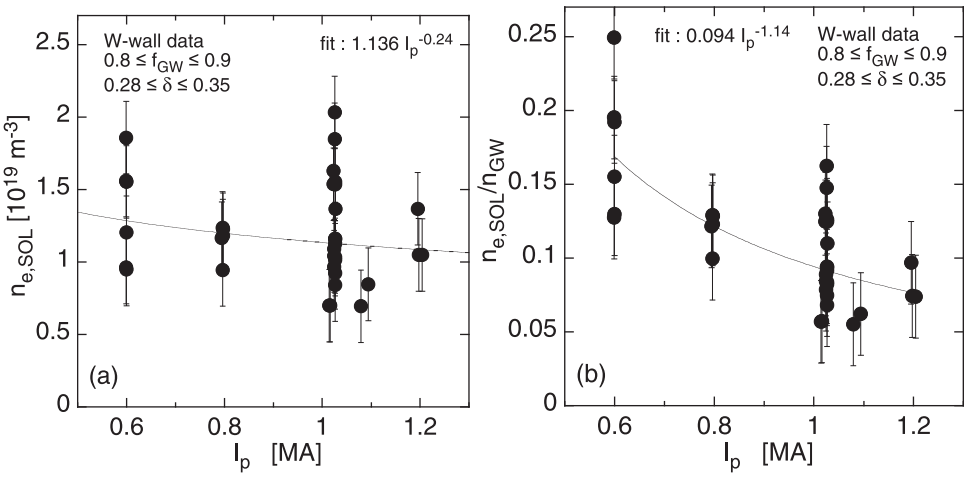

Figure 16. Dependence of $n_{e,SOL}$ and $n_{e,SOL}/n_{GW}$ on I_p for the W data in the ranges indicated in the plots. The lines are the power fits indicated in the plots.

increases proportionally to I_p per definition, the required particle source remains almost constant. This is attributed to the fact that particle confinement increases with plasma current.

For completeness and comparison with the analyses in JET [4], we note that using $n_{e,SOL}/n_{GW}$ instead of $n_{e,SOL}$ for regressions of the present AUG data, has almost no impact the exponents α_{B_T}, $\alpha_{P_{loss}}$ and α_δ indicated in table 2 while α_{I_p} increases by about 0.25.

The analysis presented above suggests that, in AUG, $n_{e,SOL}$ might be a better suited approximation of the particle source than $n_{e,SOL}/n_{GW}$ in such investigations. Some confirmation on this issue can be gained from a comparison with two other quantities linked to edge particle source such as divertor neutral gas pressure and fuelling rate, when the latter is representative of the situation. In fact, while figure 12 yields a good correlation between P_{div} and $n_{e,SOL}$, a similar plot using $n_{e,SOL}/n_{GW}$ (not shown) tends to exhibit good correlation for each value of I_p but only on separated branches, one for each current. Similar differences are found when comparing $n_{e,SOL}$ and $n_{e,SOL}/n_{GW}$ plotted versus fuelling rate for the time points corresponding to steady-state for particle confinement.

It is however essential to emphasise that these results suggesting that $n_{e,SOL}$ yields a more consistent picture of the density behaviour than $n_{e,SOL}/n_{GW}$ are deduced here in a *single device* and thus do not prove that $n_{e,SOL}$ is adequate for inter-machine comparison. Indeed, the analysis reported in [25] combining AUG and JET data indicated that $n_{e,SOL}/n_{GW}$ is a good variable for multi-machine comparison. The study on the H–L transition in AUG and JET presented recently in [61] suggests that $n_{e,sep}/n_{GW}$ is an appropriate parameter to unify the occurrence of the H–L in these two devices. It might be desirable to further investigate this subject in future investigations combining several devices.

4. Comparison of the confinement data to the IPB98(y,2) scaling

In this section we present characteristics of the confinement time yielded by this dataset in comparisons to the IPB98(y,2) confinement time scaling to connect with the previous results. During the last two decades, the reference for the thermal confinement time was τ_{th} yielded by the widely used scaling

expression IPB98(y,2) [1] table 5, which reads:

$$\tau_{\mathrm{IPB98(y,2)}} = 0.0562 I_{\mathrm{p}}^{0.93} B_{\mathrm{T}}^{0.15} n_{\mathrm{e}}^{0.41} P_{\mathrm{loss}}^{-0.69} R^{1.97} \times \kappa^{0.78} (a/R)^{0.58} M_{\mathrm{eff}}^{0.19} \quad (2)$$

where κ is the plasma elongation and M_{eff} the averaged ion mass. The respective units are: MA, T, 10^{19} m^{-3}, MW, m. The ratio $\tau_{\mathrm{th}}/\tau_{\mathrm{IPB98(y,2)}}$ yields the widely-used $H_{98(y,2)}$ enhancement factor. As discussed in [3], the IPB98(y,2) scaling expression is believed to take the I_{p} and P_{loss} dependences rather correctly into account for usual H-modes but the positive B_{T} exponent does not agree with the recent results. It is also important to note that $\tau_{\mathrm{IPB98(y,2)}}$ has a positive density dependence which is not in agreement with the actual, much weaker dependence, observed in the large diverted tokamaks. In addition to assessing the possible impact of metallic walls on confinement, the density dependence also was one of the motivations to upgrade the ITPA confinement database with new data from AUG (the present paper) and JET [4], as these new datasets contain more high density plasmas. It should also be underlined that the impact of triangularity is not included in IPB98(y,2). Indeed, as recognised long ago in several tokamaks, in AUG [65] and JET [66] as well, triangularity plays a positive role for confinement whereby, in particular when density is pushed to high values with gas puffing, higher confinement time can be sustained thanks to higher triangularity. A positive dependence on triangularity is indeed confirmed in the recent analysis of the international multi-machine database [3] and JET database [4].

Increasing density by gas puffing induces a flattening of the density profile just outside of the separatrix as reported in [59, 60]. In addition, as already mentioned above, the density profile is gradually shifted outwards which reduces the pedestal stability and the pressure at the pedestal top [36, 38]. This induces a reduction of the plasma energy and therefore lowers the confinement time. This effect of confinement degradation has recently been confirmed in full plasma integrated modelling [67]. The impact of triangularity and SOL in this frame are discussed in more details below.

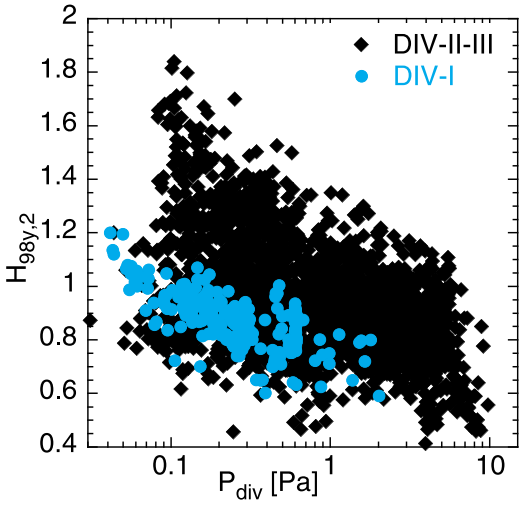

Figure 17. $H_{98(y,2)}$ versus neutral gas pressure in divertor for the data obtained with Div-I and Div-II and Div-III.

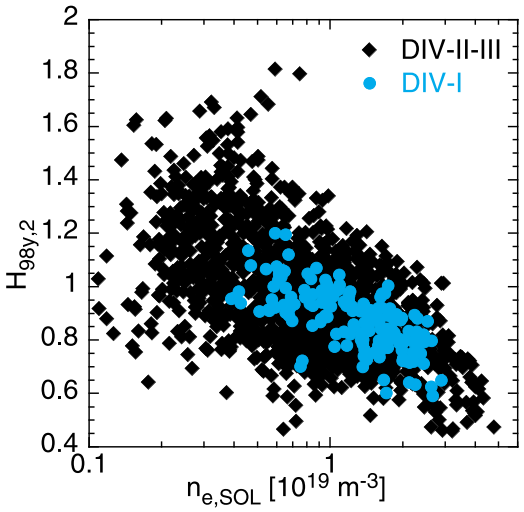

Figure 18. $H_{98(y,2)}$ versus $n_{\mathrm{e,SOL}}$ for the data obtained with Div-I and Div-II and Div-III.

4.1. Impact of the divertor geometry

We investigate here a possible direct or indirect impact of the divertor geometry on confinement by comparing confinement for the open Div-I and the closed Div-II and Div-III. As shown above in figure 12, the open and closed divertor geometries are reflected by different values of $n_{\mathrm{e,SOL}}$ for the same neutral gas density in the divertor. Figure 17 indicates that for a given value of P_{div}, $H_{98(y,2)}$ is clearly lower for Div-I.

However, as shown in figure 18, plotting $H_{98(y,2)}$ versus $n_{\mathrm{e,SOL}}$ brings the data from the two divertor configurations to a common pattern, suggesting that $n_{\mathrm{e,SOL}}$ is a more adequate parameter than the divertor neutral gas pressure. This is therefore also in agreement with the effect of the density profile on the pedestal stability mentioned just above.

In summary, the neutral retention factor of a divertor, which is strongly determined by the divertor geometry but possibly also by the shape of the magnetic configuration with respect to the divertor geometry, plays indirectly a key role for confinement through the impact of the density profile in the SOL and pedestal regions. Thus, $n_{\mathrm{e,SOL}}$ provides a good unification of the confinement data obtained with the different divertor configurations. It should be underlined that the positive effect of divertor gas retention on confinement has been reported three decades ago for the ASDEX tokamak [68].

4.2. Confinement in the C-wall and W-wall

It is well-known that the wall conditions, through material or coating, influence confinement, for instance due to change of recycling and its impact on the SOL and edge density, see e.g. [69] for AUG. It is therefore instructive to separate the periods of time with C-wall and W-wall in AUG. A first overview is provided by plotting $H_{98(y,2)}$ versus the Greenwald density fraction f_{GW} in figure 19 in which the C and W periods are indicated with different symbols.

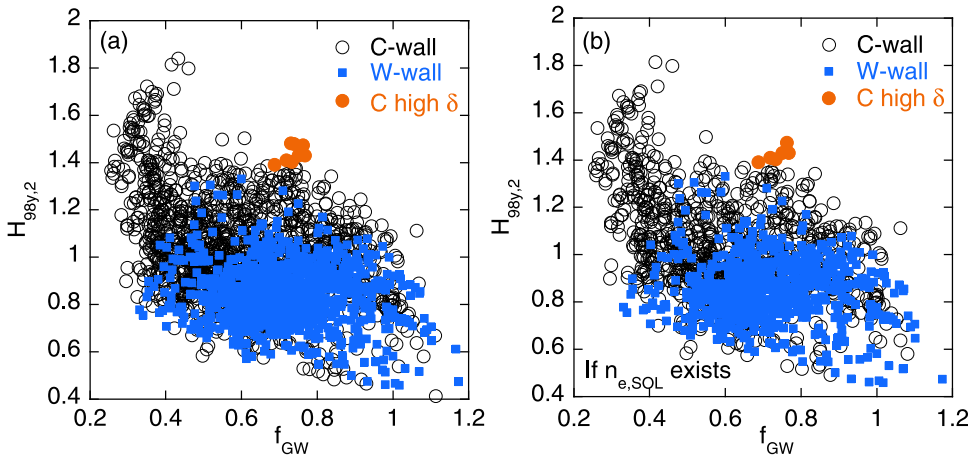

Figure 19. $H_{98(y,2)}$ versus f_{GW} for C and W walls. Plot (*a*) for all the data, plot (*b*) for data when $n_{e,SOL}$ exists. As example to illustrate the impact of $n_{e,SOL}$ a selection of eight points with good confinement at high δ are highlighted with solid circles for comparison with figure 20.

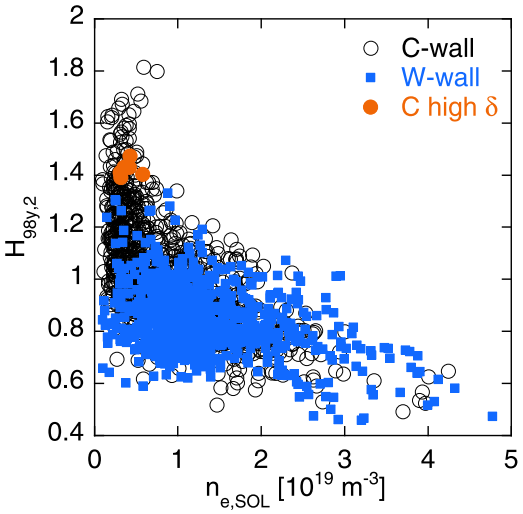

Figure 20. $H_{98(y,2)}$ versus $n_{e,SOL}$ showing the overlap of the C and W wall data. The selection of points at high triangularity from figure 19 are shown here also by the solid circles.

This figure contains two plots: plot (*a*) taking into account all the data points and plot (*b*) only data for which $n_{e,SOL}$ exists. The latter is shown in preparation for the next figure 20 and indicates that the general behaviour is not distorted by the absence of the points for which $n_{e,SOL}$ is not available. In these plots, the upper left corner is only populated by points from the C-wall period for the reasons indicated above, where the best confinement arises from HYBRID-C as shown in the next sub-section. The C-wall and W-wall data points exhibit a rather good overlap for $f_{GW} \geqslant 0.6$ with a trend for the W-wall points to be somewhat lower. The overall decrease of $H_{98(y,2)}$ with f_{GW} is mainly due to the positive n_e dependence of the IPB98(y,2) scaling mentioned above. Therefore the database reflects the general knowledge and experience with the C and W walls in AUG. In addition, in these two plots a selection of eight C-wall points at high δ and rather high f_{GW} with very good confinement are indicated by solid circles to illustrate the effect of $n_{e,SOL}$ in the next figure.

Figure 20 shows $H_{98(y,2)}$ versus $n_{e,SOL}$, here also for the C and W walls. Overall, it indicates that the best confinement values are obtained at low values of $n_{e,SOL}$, which do not necessarily correspond to low line-averaged density. The poorest confinement points correspond to high $n_{e,SOL}$ values. Furthermore, $n_{e,SOL}$ seems to unify the data from C and W wall rather well as both datasets exhibit very similar patterns and a good overlap, even if very high confinement, characterised by a high T_i/T_e ratio, is only obtained in the C-wall at very low values of $n_{e,SOL}$. As mentioned above, access to this region is hampered by W accumulation in the W-wall. The selected points at high δ (solid circles) are found at very low $n_{e,SOL}$ despite their rather high f_{GW} and are therefore consistent with the other points with similarly good confinement. It must be underlined that the vertical scatter is very large at low values of $n_{e,SOL}$ ($n_{e,SOL} \leqslant 0.8 \times 10^{19}$ m^{-3}) but it decreases strongly for larger values of $n_{e,SOL}$. We will analyse this effect in more details in section 6. Overall this figure confirms the key positive role played by low $n_{e,SOL}$ together with high δ for confinement: as indicated above by figure 15 high density can be reached at high δ with low value of $n_{e,SOL}$, corresponding in practice to low gas puff rate. Such a situation is positive for confinement but critical for W accumulation and a well-chosen amount of central ECRH is required.

It is worth underlying that the JET results shown in figure 11 of reference [4] exhibit similarities on the relation between confinement and $n_{e,SOL}$ or $n_{e,sep}$.

4.3. Confinement of the different scenarios

As indicated in the previous section three types of scenarios are considered in the ITPA database, which are also represented in the AUG database: ELMy H-modes, improved H-modes (HYBRID-C and HYBRID-W) and ITER BL. As indicated above we add here the category CDH. The confinement properties of these scenario classes are compared in figure 21 by plotting $H_{98(y,2)}$ versus f_{GW} in panel (*a*).

The HYBRID-C points reach the highest confinement values at low density and in particular populate the upper left corner. The HYBRID-W are at higher f_{GW}, some of them

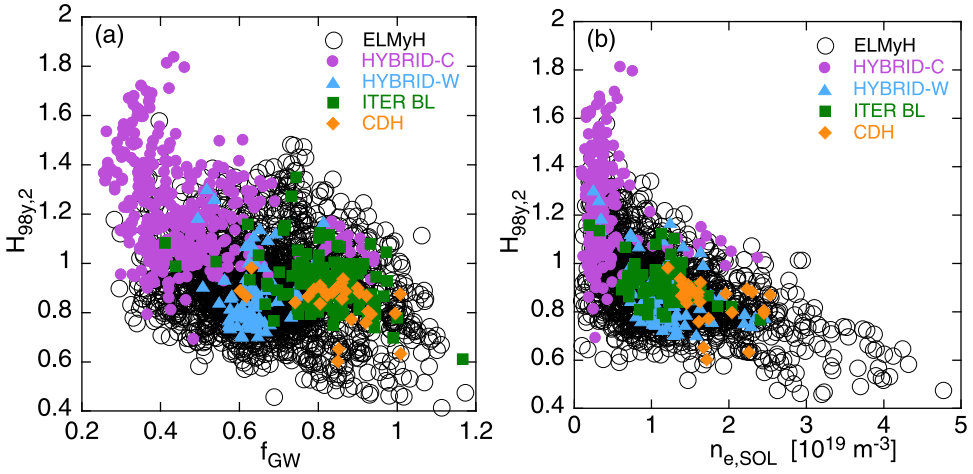

Figure 21. Comparison of the confinement properties of the ELMy H-mode, HYBRID-C, HYBRID-W and ITER BL discharges. The enhancement factor $H_{98(y,2)}$ is plotted versus Greenwald fraction in plot (*a*) and versus SOL density in plot (*b*).

reach $H_{98(y,2)}$ up to about 1.2 and have therefore quite good confinement, which is indeed the aim of the experiments, see [34, 52, 54] for more details. The ITER BL points are all at rather high density with on average good confinement as expected from the high triangularity. The CDH points exhibit confinement with $H_{98(y,2)}$ values in the region below unity and poorer than ITER BL and HYBRID-C. The ELMyH points cover the largest part of the plot, except very low density with very high confinement. Overall, for f_{GW} above roughly 0.5 the confinement for all scenarios overlaps. This does not mean that the discharges are identical, they cover at least partly different regions in the operation space, but have similar normalised confinement, which is indeed the purpose of the confinement scaling. Plotting $H_{98(y,2)}$ versus $n_{e,SOL}$ is shown in panel (*b*) which exhibits a clear difference compared to plot (*a*): for $n_{e,SOL}$ above 1.0×10^{19} m^{-3} the vertical scatter is much smaller that in the plot versus f_{GW} indicating that $n_{e,SOL}$ plays a significant role in ordering the data. The best confinement is obtained at very low values of $n_{e,SOL}$ mainly through the HYBRID-C points. Note however the presence of three HYBRID-W points in the same region with $H_{98(y,2)}$ around 1.2. In fact, almost all the attempts for HYBRID-C recorded in this database are grouped in a quite narrow $n_{e,SOL}$ range, but with a large variation in confinement, including confinement with $H_{98(y,2)}$ as low as 0.8. The corresponding range in f_{GW} for the HYBRID-C data is not as narrow as that in $n_{e,SOL}$ and the difference corresponds to the results presented in the previous section: triangularity plays a role and the f_{GW} value is very sensitive to $n_{e,SOL}$ in the low value range, see figure 15(*a*).

Despite their rather high Greenwald factor (see plot (*a*)), the ITER BL points are found in the lower half of the $n_{e,SOL}$ range which is consistent with their rather higher triangularity and explains their rather good confinement. The confinement of the CDH points is comparable to that of the ITER BL while the values of $n_{e,SOL}$ of both scenarios are similar. The ELMy H-modes cover here also a large part of the space, including the high $n_{e,SOL}$ with low confinement region, which is not populated by points from the other scenarios. This plot also shows that $n_{e,SOL}$ orders well the points of these scenarios, as well as the points for each scenario. This plot clearly exhibits a relation between confinement degradation and increasing $n_{e,SOL}$, but the overall pattern of the points has a rather triangular shape with a large vertical scatter at low values of $n_{e,SOL}$. This will be investigated in more details in the next section.

5. Analysis of the energy confinement time properties

After having compared the AUG confinement time data to the IPB98(y,2) scaling, in this section we analyse them by means of regressions and specific investigations which show that some of the dependences obtained from this dataset are significantly different from those of the IPB98(y,2) scaling expression, but close to ITPA20-IL.

This section is the core of the analyses of the confinement time properties as deduced from the database and different aspects are presented in the next sub-sections, as follows:

- 5.1 Calculation of the pairwise correlation coefficients between the regressors to find the variables which are strongly correlated and could yield misleading results;
- 5.2 Regressions made for the C and W datasets separately when the correlation values allow. The number of regressors is increased step by step to investigate their respective impact whereby in particular triangularity is also taken into account. This yields several expressions which can be used according to the aim of the comparison with the experimental data;
- 5.3 Discussion of the I_p and B_T dependences;
- 5.4 Comparison of confinement data obtained in the C and W walls;
- 5.5 Analysis of the impact of electron heating, mainly ECRH: the data exhibit its unfavourable effect in the low density range;
- 5.6 Discussion of the scatter of the confinement data, mainly due here to electron heating and the presence of the residual helium concentration mentioned above;

- 5.7 Role of $n_{e,SOL}$: this quantity plays a role in confinement by its impact on the edge density profile and pedestal stability;
- 5.8 Comparison of the confinement for the four classes of scenario specified above. The differences between them are modified compared to those exhibited by $H_{98(y,2)}$ which is mainly due to the different density dependence and the impact of triangularity;
- 5.9 Comparison of the operational region and confinement properties for different ELM types.

5.1. Correlation between the regressors

Before performing the regressions it is important to assess the possible pairwise correlations between the regressors[1]. As shown in the next sub-sections the regressors to be considered here are $I_p, B_T, P_{loss}, n_e, \delta$. The correlation coefficients between these quantities have been investigated separately for C and W wall yielding the values reported in table 3. The correlation coefficients indicated in this table are calculated pairwise for the regressors according to the usual definition of the correlation between two quantities. They quantifies the degree of relationship between these two quantities, definition and further details can be found on the jmp website of the SAS company [70].

This table indicates that the C-wall dataset is well conditioned with the two strongest correlations being 0.48 between I_p and n_e, followed by (I_p, B_T) with 0.37, values which are in general not considered to very strongly impact on the results of the regressions.

The (I_p, n_e) correlation is mainly due to two reasons. Firstly the lowest density tends to clearly increase with I_p through particle confinement. Secondly the upper limit of n_e which is generally reached with gas puffing is determined by n_{GW} which is proportional to I_p. Thus both the lower and upper boundaries for n_e are correlated with I_p. This natural correlation can be only partly reduced by lowering as much as possible n_e in the low density operation, for instance through wall conditioning, reducing as much as possible recycling and limiting the gas puffing to the strict minimum, in many cases already right at the start of the discharge.

The (I_p, B_T) correlation arises on one hand from highest value $B_T = 3.07$ T contained in the database, whereby the highest values ever used in AUG is 3.2 T for a few discharges, and on the other hand from the physics limitations, e.g. the lowest possible value of q_{95} being around 3 which determines the lowest B_T value for a given I_p. This is reflected by figure 22 which displays the distribution of the low B_T ($B_T \leqslant 1.5$ T) and high B_T values ($B_T \approx 3$ T) as a function of I_p. The lower B_T values are concentrated at low plasma current, while the points around 3 T are found at high values of I_p which explains the correlation.

For the W-wall dataset there is a very strong correlation of 0.82 between I_p and n_e which is due to the fact that low densities are not accessible with the W-wall due to W accumulation, as discussed in the previous section and documented by figure 3. In the W dataset there are in addition several moderate correlations which might play some role: (B_T, δ) at 0.46, (δ, P_{loss}) at 0.38, (n_e, B_T) at -0.37 and (δ, n_e) at 0.32. Therefore the W dataset is not well conditioned and only few regressions yield meaningful results.

[1] The correlations and regressions are calculated with the statistics programme *jmp* provided by the SAS company.

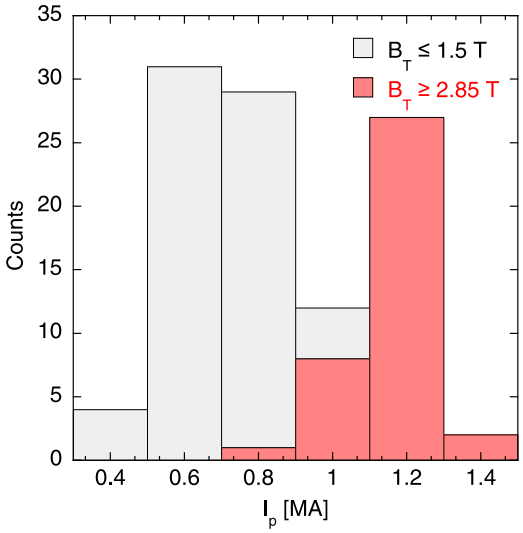

Figure 22. Distribution function of the lower and higher values of B_T versus plasma current. The highest I_p value of 1.4 MA is determined by the machine limits.

Table 3. Matrix of the pairwise correlation coefficients between the quantities used in the regressions.

	I_p	B_T	P_{loss}	n_e	δ	Wall
I_p	1.0					C
B_T	0.37	1.0				C
P_{loss}	0.26	0.03	1.0			C
n_e	0.48	−0.14	0.27	1.0		C
δ	−0.09	−0.29	0.19	0.25	1.0	C
I_p	1.0					W
B_T	−0.07	1.0				W
P_{loss}	0.25	0.03	1.0			W
n_e	0.82	−0.37	0.24	1.0		W
δ	0.09	−0.46	0.38	0.32	1.0	W
I_p	1.0					C+W
B_T	0.11	1.0				C+W
P_{loss}	0.20	0.07	1.0			C+W
n_e	0.59	−0.20	0.26	1.0		C+W
δ	−0.11	−0.19	0.27	0.27	1.0	C+W

5.2. Regressions for the energy confinement time data

To investigate the dependence of τ_{th} on the main quantities we performed regressions, here also based on the power law model and performed as least square fits on logarithmic scale, in the same way as indicated by equation (1) but with the appropriate set of regressors. This corresponds to the ordinary least square method used in [3] which yielded ITPA20-IL.

The regressors considered here are $I_p, B_T, P_{loss}, n_e, \delta$, but not the other geometric quantities which do not vary much in a single device. We performed regressions of the C and W datasets

Table 4. Summary of the regressions for τ_{th} for C and W wall datasets including different regressors. Units are seconds, MA, T, MW, 10^{19} m^{-3}. The column τ_{ref} gives the values of the confinement time yielded by the fits for usual parameters in AUG: $I_p = 1$ MA, $B_T = 2.5$ T $P_{loss} = 10$ MW, $n_e = 9 \times 10^{19}$ m^{-3} (corresponding to $f_{GW} \approx 0.8$) and $\delta = 0.3$. The labels of the rows are self-explaining, but also specified in the text. 5C+W-B_T means that α_{B_T} = has been imposed to be -0.223, the value from row 5C. The rows labelled IPTA refer to the results obtained with the WLS method for the ELMy ITER-like data subset in [3] tables 9 and 10. Here we do not include the dependences on R, ϵ, κ and M of the ITPA regressions and therefore also do not include the numerical factor which would be misleading as indicated by n/a for not applicable.

Label	ζ	α_{I_p}	α_{B_T}	α_{n_e}	$\alpha_{P_{loss}}$	α_δ	$\alpha_{1+\delta}$	RMSE	τ_{ref} (s)
1C	0.300	1.455			−0.660			0.185	0.066
1W	0.242	1.420			−0.611			0.138	0.059
2C	0.406	1.560	−0.360		−0.667			0.178	0.063
2W	0.323	1.412	−0.344		−0.609			0.132	0.058
3C	0.436	1.589	−0.384	−0.030	−0.663			0.178	0.062
3C+W	0.482	1.597	−0.467	−0.066	−0.660			0.166	0.059
ITPA IL no δ	n/a	1.311	−0.178	0.157	−0.634				
4C	0.630	1.570	−0.157		−0.740	0.300		0.142	0.069
4C+W	0.590	1.600	−0.360		−0.734	0.201		0.155	0.061
5C	0.803	1.660	−0.223	−0.096	−0.730	0.310		0.140	0.068
5C+W	0.870	1.725	−0.435	−0.153	−0.716	0.231		0.151	0.061
5C+W-B_T	0.699	1.687	−0.223	−0.116	−0.729	0.237		0.154	0.062
6C	0.369	1.692	−0.241	−0.122	−0.723		1.714	0.141	0.067
6C+W	0.471	1.736	−0.416	−0.168	−0.718		1.361	0.150	0.061
ITPA20-IL	n/a	1.291	−0.134	0.147	−0.644		0.560		

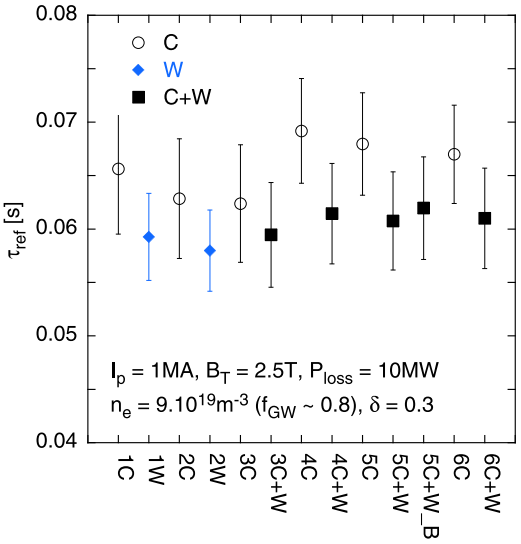

Figure 23. Values of τ_{ref} for the different regressions as listed in table 4. The error bars correspond to the one RMSE given in the table.

separately to investigate the dependences of confinement on the usual parameters. The number of regressors included in the various regressions has been increased one after the other to assess their possible influence on the other dependences. The results are given in table 4. Each row is labelled with a number and C, W or C+W depending on the dataset which was used. The columns give the values of the exponents for each regressor. The values in the column named τ_{ref} provide the confinement time for each fit for usual values of the control parameters in AUG which are indicated in the caption of the table. The values of τ_{ref} are also summarised in figure 23.

Rows 1C and 1W include only the two variables, I_p and P_{loss}, known to be responsible for the strongest dependences of the confinement time. Both rows 1C and 1W exhibit a rather strong I_p dependence ($\alpha_{I_p} \approx 1.45$) but a usual P_{loss} dependence ($\alpha_{P_{loss}} \approx -0.65$). The numerical factor for 1W is about 20% lower than that of 1C, but this difference is partly compensated by the weaker power degradation of row 1W such that, for $I_p = 1$ MA, the difference is reduced to 15% at 5 MW and 10% at 10 MW.

Including also B_T (rows 2C and 2W) reveals a clear confinement degradation with magnetic field ($\alpha_{B_T} \approx -0.35$) while the dependences on I_p and P_{loss} vary little with respect to 1C and 1W. The increase of α_{I_p} from 1.47 for row 1C and to 1.57 for row 2C is attributed to the correlation between I_p and B_T mentioned above. The difference between the C and W datasets is comparable to that of rows 1C and 1W.

The next regressor which has been included is density. This, however, can only be done for the C dataset (row 3C) and not for the W dataset for which the correlation between I_p and n_e is too high such that the regression does not yield meaningful results. It yields in particular a much weaker I_p dependence. The regression 3C exhibits a negligible density dependence while the I_p, B_T and P_{loss} dependences vary little compared to the previous cases. The exponents of a common regression for the two datasets, 3C+W, are similar to those of 3C except for α_{B_T} which is clearly more negative whose origin might be the correlation between I_p and n_e. The row 'ITPA IL no δ' gives the exponents of the corresponding ITPA regression, where IL refers to the 'ELMy ITER-like' selection, see table 9 in [3]. It exhibits a clearly weaker I_p dependence, less negative B_T and a positive impact of density. This is also the case for the regressions made for JET [4]. We note, however, that the sum $\alpha_{I_p} + \alpha_{B_T}$ is almost the same for the ITPA, JET, 3C and 3C+W regressions which is a rather general observation as pointed out in [3].

As already mentioned above, triangularity improves particle and energy confinement. Including this quantity in the regressions, excluding or including density (rows 4C, 4C+W and 5C, 5C+W respectively) reveals indeed a clear positive δ dependence. Including δ as regressor increases somewhat α_{I_p}, α_{B_T} becomes a bit less negative while the P_{loss} dependence becomes more negative, which would be very unfavourable for future device. These changes might be caused by correlations although δ is not strongly correlated with B_T and P_{loss}. Other possible reasons for these changes are not identified. For the row 5C+W-B_T the $B_T^{-0.223}$ dependence of 5C has been imposed which slightly reduces α_{I_p} in comparison to 5C+W while the other exponents vary little.

The values of τ_{ref} predicted by the different fits given in table 4 and figure 23 indicate that the regressions predict a lower confinement time for the W-data compared to the C-data the difference being about 10%. For the C+W data the τ_{ref} values are in-between with only small variations between the regressions. These regressions seem therefore appropriate to compare the C and W data and 5C+W will be used below.

Finally, in rows 6C and 6C+W of table 4 the variable used for triangularity is not δ but $1+\delta$ to allow for a direct comparison with the corresponding regression result from the ITPA multi-machine database which is given here in the last row of table 4 and is presently the ITPA 'recommended scaling' named ITPA20-IL [3]. As above, the ITPA I_p, B_T and P_{loss} dependences are weaker, the density dependence is positive and not negative, although always weak, while the effect of triangularity is clearly weaker than in AUG.

The ratio $\tau_{th}/\tau_{scaling}$ exhibits an average value close to 1 but a larger scatter when $\tau_{scaling}$ is the ITPA20-IL expression compared to the scatter when $\tau_{scaling}$ is 6C+W whereby the most important effect arises from the different dependences on triangularity. It is however noted that the other two regressions methods performed on the multi-machine database (RBAYES and GLS, see table 10 in [3]) yield single dependences which are closer to that found in AUG, such as $\alpha_{I_p} = 1.44$ and $\alpha_{B_T} = -0.22$ from RBAYES and $\alpha_{P_{loss}} = -0.73$ from GLS, both regressions with an almost negligible density dependence. Therefore, overall, the dependences yielded by our analysis of the AUG database are in general agreement with those reported for the multi-machine database, in particular if one considers the results from the three statistical methods applied in the multi-machine database.

In the next subsections we discuss some of the dependences yielded by the regressions and analyse how they impact on the interpretation and assessment of the confinement properties.

5.3. Discussion of the I_p and B_T dependences

It is instructive to have a closer look at the I_p and B_T dependences. Considering first the I_p dependence, in figure 24 we plot τ_{th} normalised by the B_T and P_{loss} dependences of the regressions 2C and 2W for the C and W wall datasets respectively. Despite the large scatter this figure suggests an off-set linear scaling with $I_p \approx 0.25$ MA for $\tau_{th} = 0$. The off-set linear fits corresponding to C and W wall data are drawn. Note that they are very close to each other over the whole I_p range.

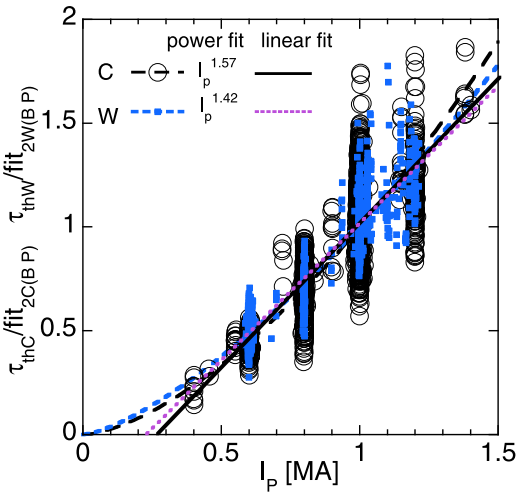

Figure 24. Confinement time normalised by the B_T and P_{loss} dependences of regressions 2C and 2W plotted versus plasma current. The different symbols indicate the data for C and W walls. Power fits and offset linear fits are plotted for each of the two datasets.

The power law fits for each dataset are also plotted yielding logically values of α_{I_p} in agreement with the results given in row 2C and 2W of table 4. They both tend to be higher than the data at the lowest I_p values while that for the C dataset tends to be higher than the other three fits for $I_p = 1.4$ MA. This figure explains why α_{I_p} is clearly larger than unity but also asks the question whether a power law assumption is the most appropriate approach for the plasma current dependence, in particular in view of extrapolation for future large devices. Such an I_p dependence with α_{I_p} larger than unity was already reported in earlier analyses of AUG confinement data for the C-wall only [26], such that these results are not in contradictions with previous ones. A similar behaviour is found in the analysis of the multi-machine ITPA database as shown by plot (*a*) of figure 6 in [3]. It is also worth mentioning that when the pedestal and core contributions to plasma energy, W_{ped} and W_{core} respectively, are fitted separately as described for the 'two-term scaling' in [71], the exponents of the I_p dependences are found to be $I_p^{1.58}$ for W_{ped} and $I_p^{0.88}$ for W_{core}. For AUG standard parameters this scaling yields an $I_p^{1.2}$ dependence, which is however quite sensitive to the relative contributions of W_{ped} to plasma energy. Former investigations of the increase of the pedestal top pressure in AUG exhibited a strong I_p dependence [62]. Thus, the strong I_p dependence found in AUG seems to be strongly determined by the pedestal behaviour.

All our regressions (table 4) indicate a non-negligible negative B_T dependence which is in strong contrast to that of the IPB98(y,2) scaling but in rough agreement with those found for JET [4] and for the multi-machine database [3]. To assess it, we consider τ_{th} normalised by the regressions 1C and 1W, which do not include B_T as regressor, and plot it versus B_T, as shown in figures 25(*a*) and (*b*) for C and W respectively. The power law fits made under these conditions are also plotted. The values of α_{B_T} obtained from these plots are somewhat less negative than those yielded by the regressions in which the fit is optimised by the procedure taking into account the

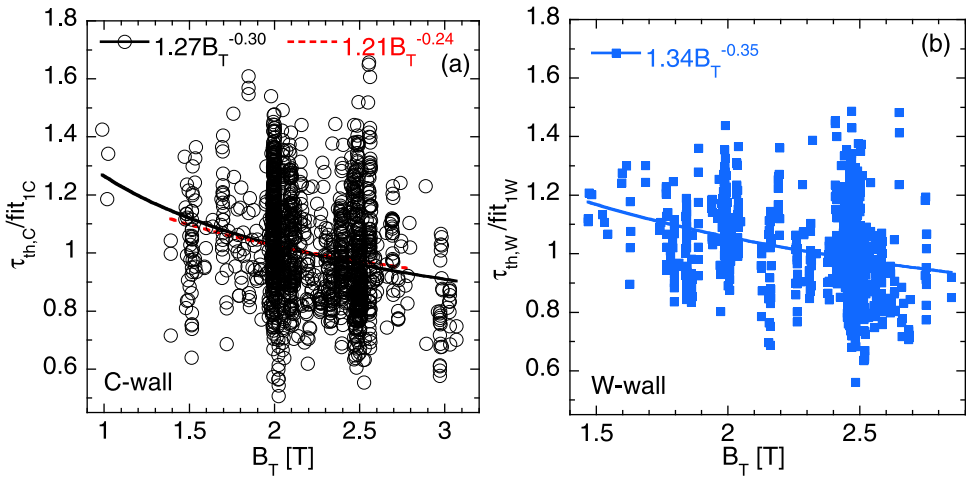

Figure 25. τ_{th} normalised by the respective fits for C and W wall as a function of B_T. Plot (*a*) for C-wall indicating two fits to the data: solid line all data taken into account, dashed line for limited B_T range, $B_T = 1$ T and $B_T = 3$ T excluded. Plot (*b*) data for the W-wall, the existing B_T of the data points is narrower 1.5–2.8 T.

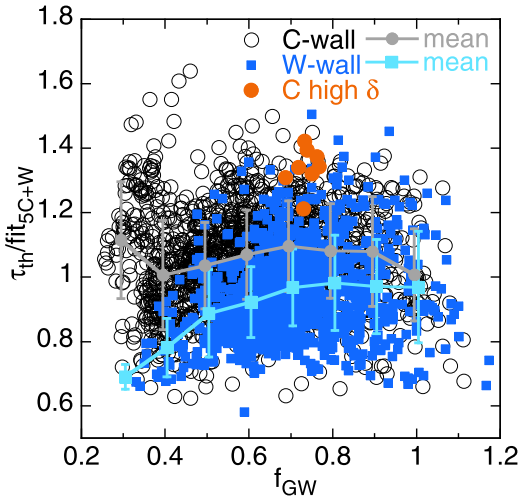

Figure 26. τ_{th} normalised by the fit_{5C+W} for C and W wall as a function of f_{GW}. The lines correspond to the mean for the C and W data calculated in adjacent intervals of f_{GW} and the error bars represent the standard deviation for each of these values. The few selected points at high δ already shown in figure 19 are also highlighted there.

other regressors. Excluding the extremes of B_T (1 T and 3 T) for the C-wall (plot (*a*)) reduces somewhat the B_T dependence. These fits confirm that the B_T dependence is indeed negative and is not caused by spurious effects when B_T is included as regressor.

The physics origin of the B_T dependence on the confinement time is not clearly identified. In addition to possible effects in the plasma core, one may speculate that it arises from the pedestal stability which is improved by higher β through the Shafranov shift, as described in [36, 37]. Indeed, in the present dataset β increases with decreasing B_T which would be in agreement with the negative α_{B_T}. Dedicated experiments performed very recently in AUG on this topic indeed confirm a clear negative B_T dependence, the analysis is currently being carried out [72].

We underline that regressions made in limited range of the safety factor, even as narrow as $3.0 \leqslant q_{95} \leqslant 5$, yield for all regressors dependences which are very similar to those reported in table 4. Along the same line, regressions made on data subsets in which the heating power have been restricted, e.g. $3 \leqslant P_{loss} \leqslant 10$ MW, yield for all the exponents values which are very similar to those obtained on the whole dataset.

Thus, it seems that the present database clearly yields a strong I_p dependence $\alpha_{I_p} \approx 1.55 \pm 0.1$ and a negative B_T dependence $\alpha_{B_T} \approx -0.25 \pm 0.1$ which however cannot be assessed with more accuracy. The density dependence is small in all the cases and that of triangularity is positive with $\alpha_\delta \approx 0.25 \pm 0.05$.

5.4. Confinement of plasmas with the C and W walls

The regressions for combined C and W (rows 3C+W, 4C+W and 5C+W) provide a common basis for comparisons between the C and W datasets. The expressions for fit_{5C+W}, which takes the largest number of regressors into account can be used to normalise τ_{th} for both the C and W data.

The result is shown in figure 26 which displays $\tau_{th}/\text{fit}_{5C+W}$ as a function of f_{GW}. The eight high δ points highlighted in figure 19 are also shown here. Here also they have good confinement but are less prominent compared to the others which is partly due to the δ dependence in fit_{5C+W}. The values of the mean and standard deviation calculated in adjacent f_{GW} windows of width 0.1 are also plotted. Note that $\tau_{th}/\text{fit}_{5C+W}$ does not decrease with increasing f_{GW} which is in contrast to the behaviour of $H_{98(y,2)}$ shown above in figure 19 and which is due to the positive density dependence in $\tau_{98(y,2)}$. Due to the restrictions caused by tungsten accumulation mentioned above, there are few W points in the low density window ($f_{GW} \leqslant 0.5$) of figure 26 and these have a rather poor confinement, in strong contrast to the C points. For $f_{GW} > 0.5$ the C and W data exhibit a better overlap and both a very weak dependence on f_{GW} for $f_{GW} \geqslant 0.6$. However, the mean values show that the confinement in the W-wall is systematically below that in the

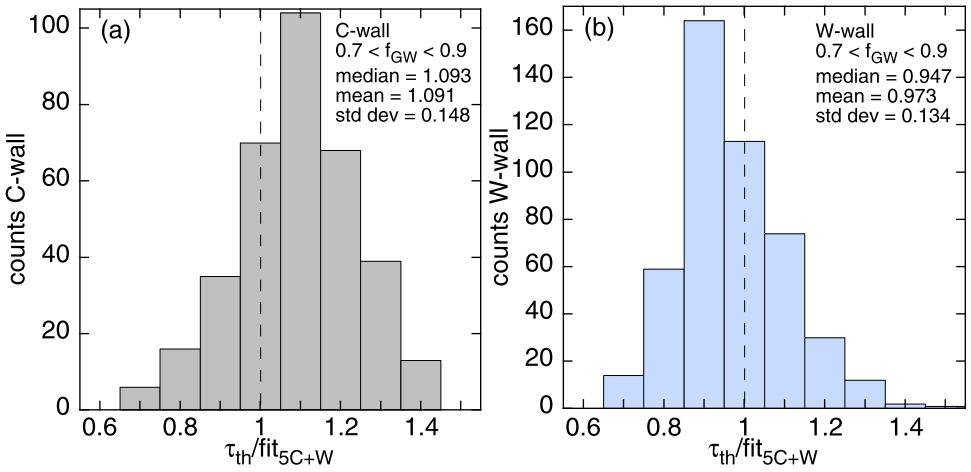

Figure 27. Distribution of $\tau_{\rm th}$ normalised by the $\rm fit_{5C+W}$ for C and W walls in the window $0.7 \geqslant f_{\rm GW} \geqslant 0.9$. The W-wall data are on averaged lower than those from C-wall according to the ratios mean-W/mean-C = 0.89 and median-W/median-C = 0.87. The standard deviations for the C and W datasets are lower than that of $\rm fit_{5C+W}$ which is 0.153.

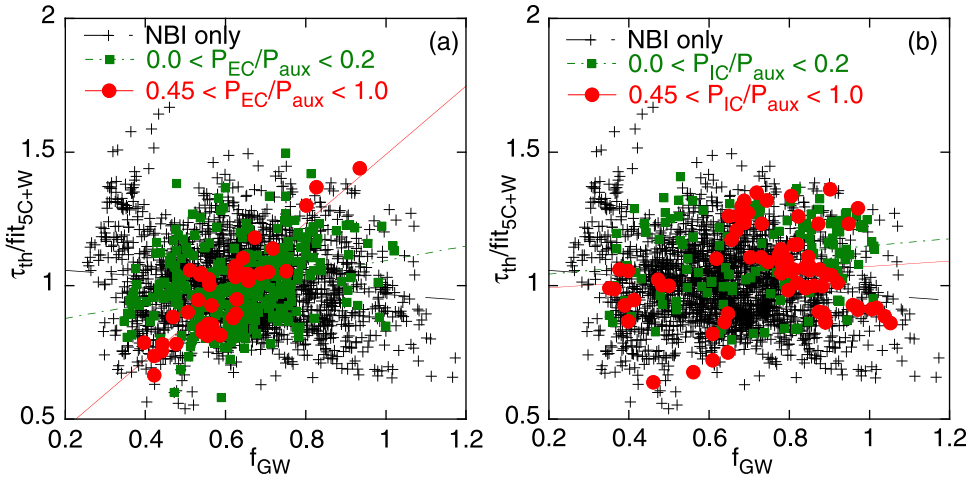

Figure 28. Effect of ECRH and ICRH on confinement in plots (*a*) and (*b*) respectively. The lines are linear fits to the corresponding sets of points.

C-wall, the difference is on average about 12%, for $f_{\rm GW} > 0.6$ but remains within one standard deviation.

An example of the data scatter and difference between C and W is shown in more details in figure 27 which displays the distributions of $\tau_{\rm th}/\rm fit_{5C+W}$ for C and W separately for data restricted to the window $0.7 \geqslant f_{\rm GW} \geqslant 0.9$. This range in $f_{\rm GW}$ is chosen because the normalised confinement for both C and W is pretty independent of $f_{\rm GW}$ there and also because this is a relevant range of $f_{\rm GW}$ for ITER. The values of the median, mean and standard deviation of the C and W distributions are indicated in the plots providing a quantitative comparison. The normalisations by fits 3C+W and 4C+W yield very similar results, with somewhat broader distributions for both C and W, but in particular for the C data for which including δ in 5C+W significantly improves the fit, as also indicated by the RMSE in table 4.

5.5. Impact of ECRH and ICRH on confinement

The regressions indicated in table 4 include the discharges with all the heating methods. It is, however, instructive to investigate the possible impact of the RF heating methods (ECRH or ICRH) on confinement. This is done in figure 28 by plotting the confinement normalised by regression 5C+W versus $f_{\rm GW}$. In each plot three different symbols represent datasets with NBI only, and with two different contributions to total heating for ECRH or ICRH as indicated by the legend. The weak decrease of confinement indicated in these plots by the fit for NBI only is due to the fact that the ECRH and ICRH heated points are not included in these fits which are therefore not quite identical to $\rm fit_{5C+W}$. Plot (*a*) illustrates the effect of the pure electron heating provided by $P_{\rm ECRH}$, showing that confinement increases clearly with density for the range $P_{\rm ECRH}/P_{\rm aux} \geqslant 0.45$. This is attributed to the fact that, in the presence of ECRH at low density the ratio $T_{\rm e}/T_{\rm i}$ can be high which destabilises the ITG turbulence [73, 74], which is deleterious for confinement, as shown in AUG experiments [50–52, 54, 75]. This effect decreases strongly with increasing density due to the stronger electron–ion energy exchange which brings $T_{\rm e}/T_{\rm i}$

close to unity. For a low contribution of P_{ECRH} to total heating, $P_{\mathrm{ECRH}}/P_{\mathrm{aux}} \leqslant 0.2$, the impact becomes significantly weaker, but the trend remains.

In contrast, plot (*b*) indicates that no clear impact of ICRH appears versus f_{GW} independently of its relative contribution. This is attributed to the fact that ICRH is not a pure electron heating. It should be underlined, however, that there are exceptions when the ICRH contribution is high at low density: the few ICRH-heated points with very low confinement in the region $f_{\mathrm{GW}} \leqslant 0.6$ correspond to $P_{\mathrm{ICRH}}/P_{\mathrm{aux}} \geqslant 0.8$.

These observations indicate that investigating the possible effect of the NBI torque on confinement should preferentially not be made for discharges with ECRH heating. However, making the analysis excluding this heating method exhibits a very large scatter and no significant trend of confinement with torque. One additional complication arises from the fact that the stronger torque provided by the two most tangential NBI beams also corresponds to a heat deposition at about mid-radius which is unfavourable for confinement. Further, due the confinement difference between the discharges in the C and W walls the C and W datasets must be analysed separately which reduces the number of points. Limiting the range in P_{loss} between 5 and 7 MW which, as shown by figure 7, provides a torque variation between 0 and 7 N m does not yield convincing results. Further investigations on this topic are out of the scope of this work.

5.6. Scatter at low f_{GW} values

The normalised confinement data in the previous figures exhibit a rather large scatter in the low density range whereby the points with high confinement correspond to the HYBRID-C discharges, see figure 21 or figure 33 below. It is however also instructive to investigate the origin of the points with poor confinement. The previous subsection indicates that ECRH contributes to poor confinement and to some extend ICRH as well. In addition, as mentioned above, the presence of helium in the plasma, even at rather low concentration, leads to deteriorated confinement [30, 31]. The analysis of these possible causes for low confinement for the present dataset yields the following set of conditions $P_{\mathrm{ECRH}}/P_{\mathrm{aux}} \geqslant 0.2$, $P_{\mathrm{ICRH}}/P_{\mathrm{aux}} \geqslant 0.8$, $P_{\mathrm{ECRH+ICRH}}/P_{\mathrm{aux}} \geqslant 0.8$ and/or [^{4}He] $\geqslant$3% which explains a large part of the poor confinement data for $f_{\mathrm{GW}} \leqslant 0.5$. This is shown by the distribution of $\tau_{\mathrm{th}}/\mathrm{fit}_{\mathrm{5C+W}}$ shown in figure 29 which indicates that the points which fulfil the above conditions (selection RF, ^{4}He) contribute strongly to the poor confinement population. At higher density these conditions do not play a clear role, in particular caused by the stronger electron–ion coupling which reduces strongly the impact of ECRH while the intrinsic helium concentration becomes small.

5.7. Role of $n_{\mathrm{e,SOL}}$

As already indicated above, see e.g. figure 20, there are strong indications that the separatrix and/or scrape-off density play a role in confinement or at least reflect conditions for poor confinement. This is also the case for the $\tau_{\mathrm{th}}/\mathrm{fit}_{\mathrm{5C+W}}$ data as shown

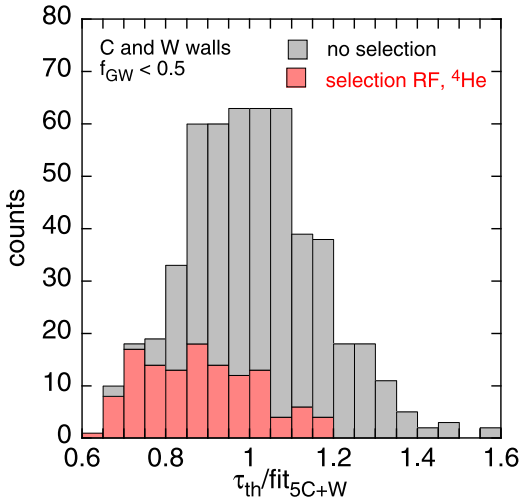

Figure 29. Distribution of normalised confinement $\tau_{\mathrm{th}}/\mathrm{fit}_{\mathrm{5C+W}}$.

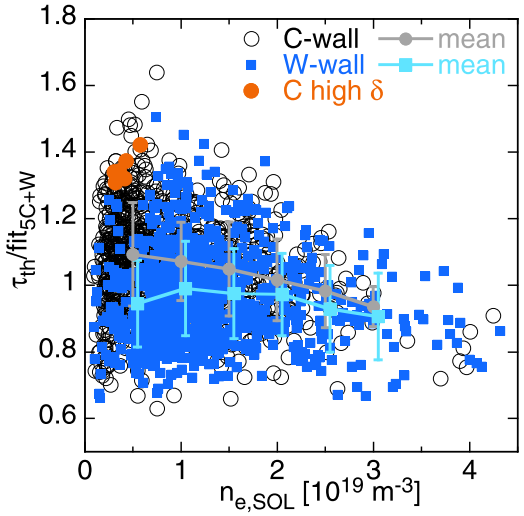

Figure 30. τ_{th} normalised by the $\mathrm{fit}_{\mathrm{5C+W}}$ versus $n_{\mathrm{e,SOL}}$ for C and W walls. The mean values for ranges of $n_{\mathrm{e,SOL}}$ of width 0.5×10^{19} m^{-3} are also indicated, the error bars correspond to one standard deviation.

in figure 30 in which the confinement normalised by $\mathrm{fit}_{\mathrm{5C+W}}$ is plotted versus $n_{\mathrm{e,SOL}}$.

The overall triangular pattern built by the points is similar to that of figure 20 ($H_{98(\mathrm{y},2)}$ versus $n_{\mathrm{e,SOL}}$), although less pronounced. Note that the selected high δ points of the previous figures also shown here (the eight full circles), at very low values of $n_{\mathrm{e,SOL}}$, are here also in the good confinement corner. The averaged decrease with increasing $n_{\mathrm{e,SOL}}$ is much weaker than for $H_{98(\mathrm{y},2)}$ mainly due to the different density dependences in $\mathrm{fit}_{\mathrm{5C+W}}$ and $\tau_{\mathrm{IPB}_{98(\mathrm{y},2)}}$. The overall scatter is somewhat smaller than in figure 20 and the C and W data exhibit a better overlap in particular at low values of $n_{\mathrm{e,SOL}}$. The overlap between the C and W data is also a bit better than when plotted versus f_{GW}, as indicated by the mean values which are close to each other and converge with increasing $n_{\mathrm{e,SOL}}$. They also indicate that the decrease with $n_{\mathrm{e,SOL}}$ is weak. This is confirmed by regressions

adding $n_{e,SOL}$ as regressor to I_p, B_T, P_{loss}, including δ and/or n_e or not. The results all yield a weak dependence close to $n_{e,SOL}^{-0.08}$.

The triangular shape of plot 30 is mainly due to the fact that the points with good confinement correspond to low values of $n_{e,SOL}$ while the boundary built by the points with low confinement is practically horizontal. Overall this indicates a confinement degradation with increasing $n_{e,SOL}$ which is mainly reflected by the decrease of the upper boundary of $\tau_{th}/\text{fit}_{5C+W}$ in this plot. Therefore this suggests that good confinement requires low $n_{e,SOL}$ values and that this is a necessary but not a sufficient condition. Vice-versa, high $n_{e,SOL}$ values always induce a confinement degradation but other factors cause low confinement at low values of $n_{e,SOL}$. In other words, the variable $n_{e,SOL}$ plays a significant role towards high density as this will be shown in more details below.

Turning now to the large scatter at low $n_{e,SOL}$. On one hand, the high to very high confinement points are mainly due to the good HYBRID-C discharges (see also figure 33). On the other hand, correspondingly to the above discussion and figure 29, we verified that the majority of the points with low confinement at low $n_{e,SOL}$ ($\tau_{th}/\text{fit}_{5C+W} \leqslant 0.8$ and $n_{e,SOL} \leqslant 1.0$) are explained by the presence of RF heating or helium. However a rather large number of points at low $n_{e,SOL}$ with $\tau_{th}/\text{fit}_{5C+W}$ between 0.8 and 1.0 remain unexplained. We looked for global parameters which would reduce the scatter of the data at low values of $n_{e,SOL}$ but did not find any clear candidate. The parameters I_p, B_T, P_{loss}, n_e, δ, already included in fit_{5C+W}, or those not included such as q_{95}, internal inductance or density peaking do not significantly better order the points in the low $n_{e,SOL}$ region. The radiation power does not explain the scatter either. Regressions applied to various data selections in limited ranges of $n_{e,SOL}$ (vertical slices in the plot) all yield results which are very similar to fit_{5C+W}.

It is also instructive to investigate in more detail the impact of $n_{e,SOL}$ in the high density region $0.7 \leqslant f_{GW} \leqslant 0.9$. This is shown in figure 31 by $\tau_{th}/\text{fit}_{5C+W}$ versus $n_{e,SOL}$. Means and standard deviations calculated for the C and W data in adjacent windows of $n_{e,SOL}$ with width of 0.5×10^{19} m^{-3} are also plotted. Due to the restriction on f_{GW}, there are very few points at very low values of $n_{e,SOL}$. The normalised confinement for both C and W exhibits a clear but rather weak decrease with $n_{e,SOL}$ which is close to $n_{e,SOL}^{-0.1}$ for both. In addition, in this f_{GW} range, the difference between the means of the C and W data is much smaller than when plotted versus f_{GW}. This shows that the impact of the edge/SOL density profile on confinement becomes gradually more important as f_{GW} is increased. This can be attributed to the impact of the outward shift of the density profile on the pedestal stability already mentioned above [36, 38], an effect which certainly increases with density.

As mentioned above, nitrogen seeding reduces the outwards shift of the pedestal density profile and causes a concomitant reduction of $n_{e,sep}$ and $n_{e,SOL}$ leading to an improvement of the pedestal stability and confinement [36]. This effect is also clearly yielded by the database. In this context, a question remains whether $n_{e,SOL}$ or $n_{e,SOL}/n_{GW}$ is the most physics relevant quantity to take into account the impact of the edge density profile on the confinement degradation at high density. For this purpose $\tau_{th}/\text{fit}_{5C+W}$ plotted versus $n_{e,SOL}$ or $n_{e,SOL}/n_{GW}$

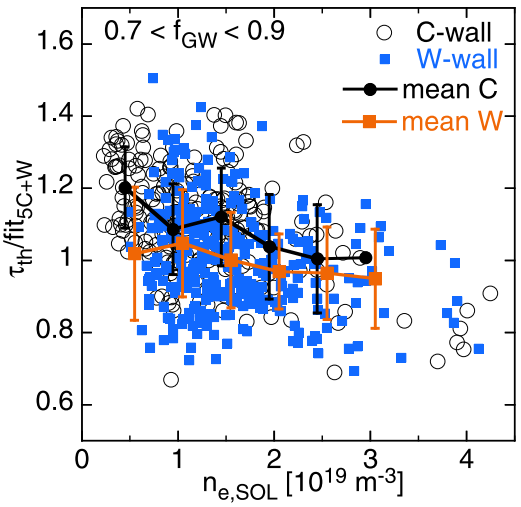

Figure 31. τ_{th} normalised by the fit_{5C+W} versus $n_{e,SOL}$ for C and W walls, restricted to the window $0.7 \leqslant f_{GW} \leqslant 0.9$.

is shown in figures 32(*a*) and (*b*) respectively, whereby the different values of plasma current are indicated with different symbols. While the data points for the different I_p values exhibit a rather good overlap, including the upper boundary, when displayed versus $n_{e,SOL}$, panel (*b*) shows that plotted versus $n_{e,SOL}/n_{GW}$ the data exhibit somewhat separated patterns for each I_p value. The difference for the points at 0.6 and 1.2 MA is very clear. As the ranges in δ and f_{GW} covered by data at the different currents are comparable (see section 2), this plot might well be representative of the behaviour.

As in section 3.2 on the role of $n_{e,SOL}$ for the density, here also we emphasise that the fact that $n_{e,SOL}$ seems to provide a more consistent picture than $n_{e,SOL}/n_{GW}$ in a single device does not imply that $n_{e,SOL}/n_{GW}$ (or $n_{e,sep}/n_{GW}$) is not better suited for multi-machine investigations. Indeed this is suggested by the rather good overlap of the AUG and JET confinement data shown in figure 5(*c*) of reference [3], whereby $n_{e,sep}/n_{GW}$ is used in this plot. Along the same line, in the work reported in reference [61] $n_{e,sep}/n_{GW}$ also brings AUG and JET together. A detailed multi-machine comparison seems highly desirable to address this question.

Overall, these analyses in AUG indicate that, for values of f_{GW} above ≈ 0.5, $n_{e,SOL}$ contributes to ordering the confinement data in addition to the control parameters included in the confinement normalisation by fit_{5C+W}. The fact that $n_{e,SOL}$ provides a better overlap of the C data with those from the W-wall which have a somewhat lower confinement is linked with the somewhat higher value of $n_{e,SOL}$ in the W-wall to reach a given value of f_{GW} mentioned in section 3.2.

5.8. *Confinement in the different scenarios*

For completeness and in comparison with the above results using $H_{98(y,2)}$, we present here the confinement properties of the scenarios in comparison with the fit_{5C+W}.

This is shown in figure 33 versus f_{GW} and $n_{e,SOL}$ in panels (*a*) and (*b*) respectively. In contrast to figure 21 where $H_{98(y,2)}$ was used there is no overall dependence on f_{GW} for

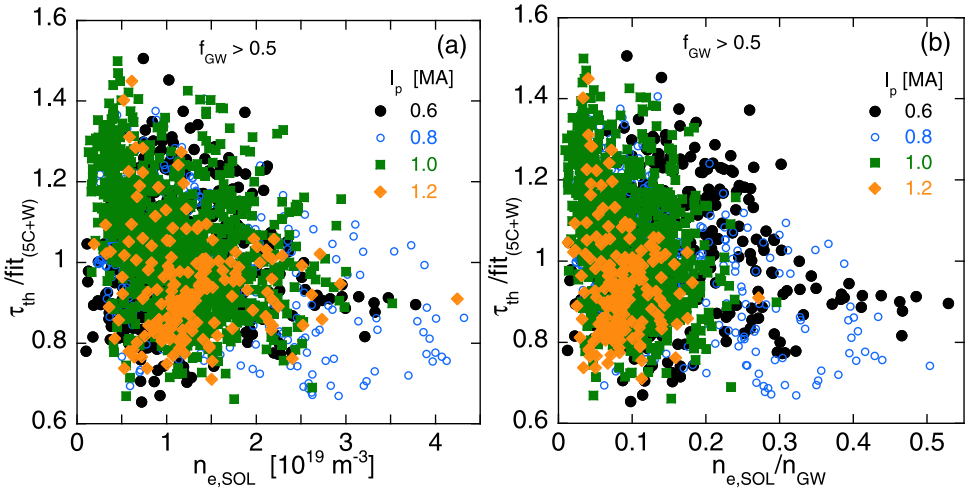

Figure 32. τ_{th} normalised by the fit_{5C+W} for C and W walls for $f_{GW} \geqslant 0.5$. Panel (*a*) versus $n_{e,SOL}$, panel (*b*) versus $n_{e,SOL}/n_{GW}$.

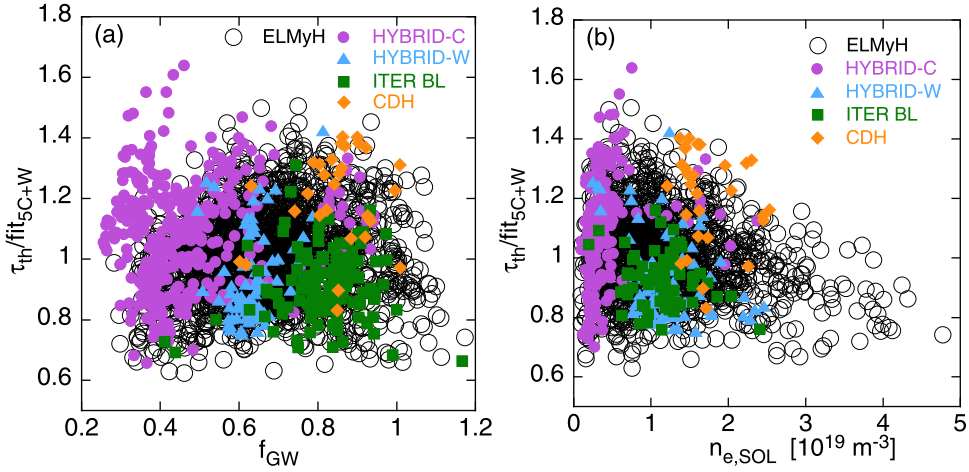

Figure 33. τ_{th} normalised by the fit_{5C+W} for the plasmas scenarios versus f_{GW} in panel (*a*) versus and versus $n_{e,SOL}$ in panel (*b*).

any of the scenarios. The relative difference in confinement between the scenarios is somewhat smaller than that exhibited by $H_{98(y,2)}$ in figure 21. The highest values of the HYBRID-C points are lower: $\tau_{th}/fit_{5C+W} \approx 1.6$ compared to $H_{98(y,2)} \approx 1.8$ and these points are overall better centred around unity. This is mainly due to the difference in the density and triangularity dependences. The distribution of $H_{98(y,2)}$ for the HYBRID-W points yields a mean of 0.89 with standard deviation of 0.13. For τ_{th}/fit_{5C+W} the mean of 0.94 is somewhat higher and with standard deviation of 0.15 the distribution is broader, there are few points with $\tau_{th}/fit_{5C+W} \approx 1.2$. For the ITER BL points τ_{th}/fit_{5C+W} yields a mean value of 0.91 with standard deviation of 0.11, very close to the values yielded by $H_{98(y,2)}$ of 0.92 and 0.11. For these points, which were performed at high I_p and δ but rather low B_T, the impact of the high density in $H_{98(y,2)}$ is replaced by that of the dependences on I_p, B_T and δ of fit_{5C+W}. Assuming the less negative B_T dependence of the C dataset, $B_T^{-0.223}$, instead of $B_T^{-0.435}$ for fit_{5C+W} brings a 0.02 increase of the mean for these points. In contrast to the plots using $H_{98(y,2)}$ the CDH points exhibit here a quite good normalised confinement, higher than ITER BL despite the rather high value of f_{GW}. This is mainly due to the positive triangularity dependence of fit_{5C+W} which enhances τ_{th}/fit_{5C+W} for the CDH discharges with low triangularity.

The representation τ_{th}/fit_{5C+W} versus $n_{e,SOL}$ shown in panel (*b*) exhibits properties which are similar to those yielded by $H_{98(y,2)}$ but the general trend to decrease with increasing $n_{e,SOL}$ is much weaker due to the weak n_e dependence in fit_{5C+W}. The differences between the scenarios are of course the same as in panel (*a*) but appear more clearly because the representation using $n_{e,SOL}$ groups the points of the different scenarios, except for ELMyH. As already seen above, the HYBRID-C points are at very low values of $n_{e,SOL}$ and exhibit the best confinement. The HYBRID-W and ITER BL points overlap clearly despite the higher f_{GW} value in the ITER BL scenario, which is mainly due to the higher triangularity of the ITER BL discharges which provides high density at low $n_{e,SOL}$. Here also, the CDH points are at the upper boundary of the confinement values for a medium value of $n_{e,SOL}$. Overall, all the good confinement points, including the ELMyH, are found for $n_{e,SOL} \leqslant 2.5 \times 10^{19}$ m^{-3}, this is also where the points from

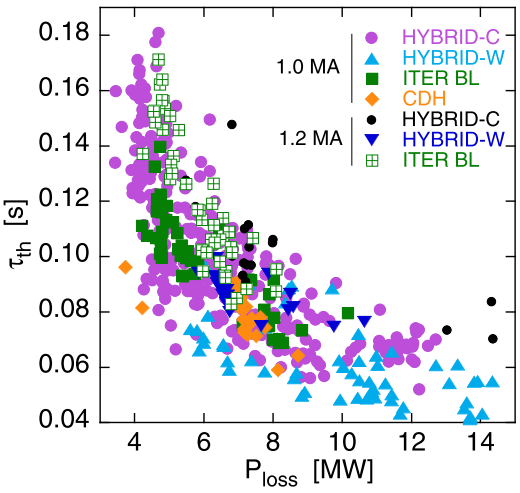

Figure 34. τ_{th} for the four plasmas scenarios at 1.0 and 1.2 MA versus P_{loss} 1.0 and 1.2 MA. The EMLyH points are not included to produce a clearer picture.

the scenarios for good confinement are located. The ELMy H-modes are found in the whole diagram, including the region with high values of $n_{e,SOL}$ where the other scenarios are absent and where confinement becomes poorer.

The confinement time normalised by a scaling is a useful quantity for comparisons between discharges but it can be somewhat misleading, in particular in comparisons between scenarios, as high normalised confinement time does not necessarily correspond to high values of τ_{th}. The absolute value of τ_{th} is therefore also important for the assessment and comparison of the quality of the scenarios. For this reason we plot in figure 34 τ_{th} versus P_{loss} for two values of plasma current 1.0 and 1.2 MA for four scenarios whereby the ELMyH points have not been included to avoid blurring the figure. This is justified by the fact that there are no ELMyH points with clearly higher confinement than the points from the four scenarios included in the plot. Considering first the points at 1.0 MA. The HYBRID-C points build the upper boundary while the HYBRID-W tend to build the lower boundary. The ITER BL are roughly in the middle. A main difference to figure 33 is that the CDH points are here just below the ITER BL ones and not clearly above them and at the higher boundary of all the points as in this previous figure. This is due to the difference in δ between these two scenarios whereby the CDH points are pushed upwards in the normalisation by fit_{5C+W} by their low δ value. The increase of I_p to 1.2 MA enhances clearly the confinement time of ITER BL, the effect is less clear for the two HYBRID categories, perhaps due to the small number of points. Note that there are no CDH discharges at 1.2 MA.

5.9. Relation between ELM type and confinement

The strong power loads released by large ELMs, in particular of type-I, must be avoided in future devices such as ITER and it is important to investigate and assess the behaviour of H-modes with small ELMs, (type-II, type-III or grassy ELMs) which might be tolerable in future fusion devices, see [76] and references therein. As mentioned above, the AUG database contains data points for ELMs of type-I, type-II and type-III. In this subsection we present a very rough estimate of the relation between ELM type and confinement. The determination of the ELM type in a large database built over more than two decades can only be very rough. In fact, identifying the actual ELM type often requires dedicated experiments and adequate diagnostics conditions which are by far not fulfiled for all the data points included in the database. For instance, if density is increased at constant heating power, type-I ELMs are very often clearly present at low density but then their frequency increases while their amplitude decreases gradually as density is increased and at some stage the ELM type might change for instance to small ELMs of type-III. However, very often the transition cannot be determined without ambiguity. It is also widely observed that in many cases type-I and type-III ELMs occur in the same time interval of a discharge without any change in the control parameters, so called 'mixed ELMs' phases. Therefore, in the present work we only distinguish two ELM categories 'large ELMs' and 'small ELMs' as also indicated by the variable PHASE (HGELM and HSELM) of the ITPA database. Historically large ELMs were labelled 'giant ELMs', small ELMs all the others. We only label time intervals as 'small ELMs' if large ELMs seem to be completely absent. However, this category does not include only very small ELMs such as type-II or grassy ELMs but also a large number of type-III ELMs which are perhaps not considered as small according to the present definition and in view of power loads in future devices. Our category 'small ELMs' is therefore much wider than the recent label 'small ELMs' which is being used in [76, 77].

According to the usual phenomenological classification, type-III ELMs appear just after the L–H transition, at heating powers just above the H-mode power threshold while type-I ELMs are observed at somewhat higher power [78]. More generally, small ELMs (type-II or type-III or grassy ELMs) appear at high edge collisionality, this means in practice high density and heating power not exceeding very much the L–H threshold power as yielded by the threshold scaling for the plasma parameters in the considered time interval. Dedicated experiments on the type-II ELMs have been carried out in AUG [77, 79–82] such that the ELM type for the corresponding discharges and time intervals included in the database can be set to type-II without ambiguity. These ELMs are obtained at rather high density, high triangularity, near double null configuration and at high collisionality.

The operational windows populated by our two ELM categories as yielded by the database are shown in figure 35. Panel (*a*) displays the ratio $P_{loss}/P_{L-H,scal08}$ where $P_{L-H,scal08}$ is the L–H threshold power yielded by the widely-used ITPA threshold scaling 2008 [83] which reads:

$$P_{LH,scal08} = 0.049 {n_e}^{0.72} {B_T}^{0.80} S^{0.94} \quad (3)$$

in MW, 10^{20} m^{-3}, T, S being the plasma surface area in m^2.

This graph indicates that for $P_{loss}/P_{L-H,scal08} \approx 1$ no small ELMs are found for values of f_{GW} below 0.45 and that this lower boundary in f_{GW} for small ELMs increases to about 0.7 for $P_{loss}/P_{L-H,scal08} \approx 5$. In the region left from this boundary only large ELMs are present which is in agreement with

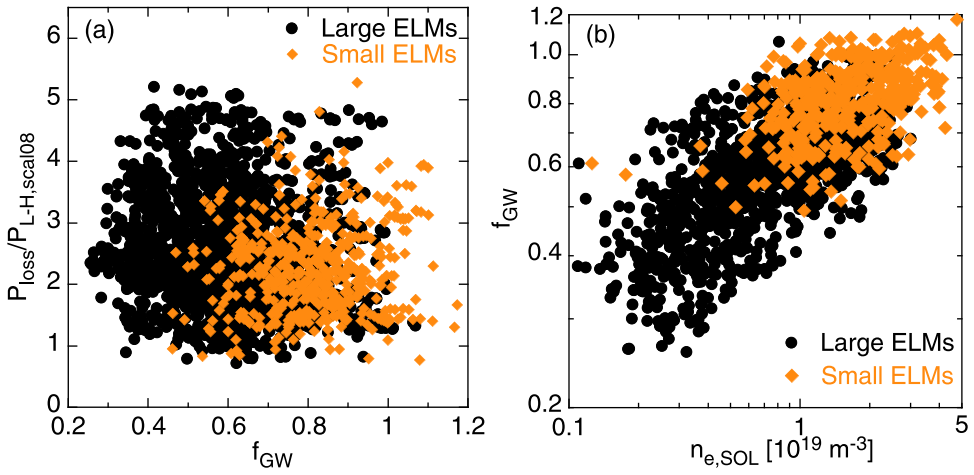

Figure 35. Operational regions of the 'large ELMs' and 'small ELMs'. Panel (*a*) $P_{\rm loss}/P_{\rm L-H,scal08}$ versus $f_{\rm GW}$. Panel (*b*) $f_{\rm GW}$ versus $n_{\rm e,SOL}$ on log–log scale.

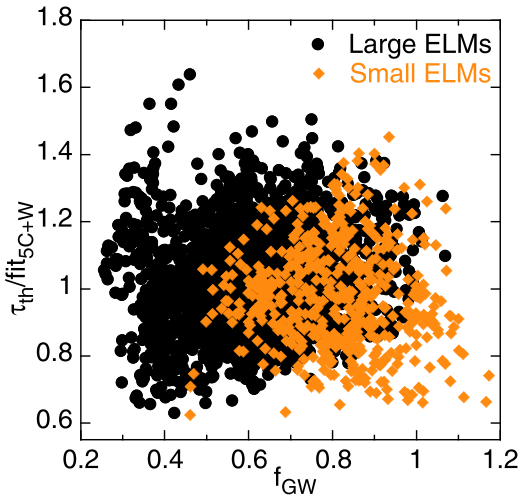

Figure 36. Confinement overview of the 'large ELMs' and 'small ELMs': $\tau_{\rm th}$ normalised by $\rm fit_{5C+W}$ versus $f_{\rm GW}$.

the usual observation that small ELMs are preferentially found at high collisionality. Thus, the small ELMs are found preferentially in the right lower corner, at high $f_{\rm GW}$ and not very high $P_{\rm loss}/P_{\rm L-H,scal08}$, although large ELMs also exist there. This overlap is due to the fact that the ELM category is not solely determined by the two parameters $f_{\rm GW}$ and low $P_{\rm loss}/P_{\rm L-H,scal08}$ and perhaps also because of the uncertainties in the determination of the ELM category as explained above. Nevertheless, the pattern exhibited by this plot is in rough agreement with the expectations. We underline here that the normalised parameters $f_{\rm GW}$ and low $P_{\rm loss}/P_{\rm L-H,scal08}$ yield a much more coherent picture than $n_{\rm e}$ and $P_{\rm loss}$.

Panel (*b*) of figure 35 indicates that large ELMs only (no small ELMs) are found at low $n_{\rm e,SOL}$ and low $f_{\rm GW}$ values while small ELMs appear at higher values of these two quantities and dominate in the upper right corner highest $n_{\rm e,SOL}$ and $f_{\rm GW}$.

The comparison of the confinement behaviour for the two ELM categories is shown in figure 36 by the normalised confinement $\tau_{\rm th}/\rm fit_{5C+W}$ plotted versus $f_{\rm GW}$. This plot exhibits clearly the patterns of the two ELM categories. Again here, large ELMs only (no small ELMs) are found in the region of lower $f_{\rm GW}$ values, whereby the upper boundary in $f_{\rm GW}$ for this region without small ELMs increases with increasing $\tau_{\rm th}/\rm fit_{5C+W}$. This behaviour might be due to the fact that higher energy confinement can also imply higher particle confinement leading to higher density without requiring necessarily more gas puffing which could degrade confinement. Referring to the above subsection 5.6 about the data scatter, we note here that the low values of $\tau_{\rm th}/\rm fit_{5C+W}$ in the window $f_{\rm GW} \leqslant 0.5$ is not due to the dominant presence of small ELMs. In contrast, small ELMs only (no large ELMs) are clearly found in the right lower corner, high $f_{\rm GW}$ and dominantly low confinement. Here also there is a large overlap of the two ELM categories between these two corners. In the range $0.7 \leqslant f_{\rm GW} \leqslant 0.9$ the averaged value of the normalised confinement for the large and small ELMs is not significantly different, as confirmed by the respective distributions (not shown) which yield a mean value of 1.040 with standard deviation of 0.141 for the large ELMs and 0.988 and 0.166 for the small ELMs. Regressions made for each of the two ELM categories yield dependences which are similar to $\rm fit_{5C+W}$ as shown in table 5.

It is also instructive to look at $\tau_{\rm th}/\rm fit_{5C+W}$ versus $n_{\rm e,SOL}$ shown in figure 37. This reveals a rather strong overlap between the domains with large and small ELMs, with the two exceptions that there are practically no small ELMs for $n_{\rm e,SOL} \leqslant 0.5 \times 10^{19}$ m^{-3} and that the small ELMs with the lowest confinement are found for the highest values of $n_{\rm e,SOL}$ which is not surprizing considering figure 36. This region with small ELMs only does not exhibit any discontinuity in confinement compared to the region on its left side. In the $n_{\rm e,SOL}$ window 1.0–2.0 10^{19} m^{-3} where both categories have a large overlap, the normalised confinement almost does not depend on the ELM category.

In summary for this subsection, there are rather limited regions where large ELMs or small ELMs only are present and a wide domain where both categories exist. Measured in comparison to the regression 5C+W, the confinement properties of the two ELM categories are comparable with only a weak trend

Table 5. Summary of the regressions for large ELMs and small ELMS including different regressors.

Label	ζ	α_{I_p}	α_{B_T}	α_{n_e}	$\alpha_{P_{loss}}$	α_δ	RMSE
Large ELMs	0.855	1.721	−0.494	−0.114	−0.722	0.222	0.145
Small ELMs	0.854	1.56	−0.187	−0.125	−0.675	0.246	0.155

for small ELMs to exhibit lower confinement. In this frame it is important to underline that comparing the confinement for large and small ELMs using $H_{98(y,2)}$ yields a clearly lower normalised confinement for small ELMs due to the positive density dependence of this scaling, see e.g. [84]. As shown for instance by the type-II ELMs studies, good confinement with very small ELMs can be achieved by the adequate choice of the plasma conditions [79, 80, 82].

5.10. Summary of the section

Several regressions could be made for the C and W data, whereas some rather strong correlations in the W-data limit the number of regressors which can be used. Regressions made for the whole dataset (C+W) yield expressions for fits which can be used for comparisons with the experimental data, done here with fit_{5C+W}. Compared to this expression the τ_{th} values of the C-data are somewhat higher and those from the W-data somewhat lower. Using this expression to normalise the confinement data for the four types of scenarios mentioned above introduces a relative shift between the scenarios in comparison to the IPB98(y,2) scaling reflecting the different density dependence and the positive impact of δ on confinement. The edge density plays a key role, probably through its impact on the edge density profile and tends to unify the confinement behaviour. The normalised confinement time for the large ELMs and small ELMs is not significantly different in the operational space where both types exist.

In the next section, some of the dependences found in this section are investigated in more detail and assessed in some subsets of the data.

6. Data at plasma current of 1 MA

To avoid possible correlations between plasma current and other quantities and therefore better assess some of the dependences, it is useful to use subsets of data for a single value of I_p which is in particular possible for 1 MA for the C-wall data. Indeed, figures 3 and 5 indicate that for the 1 MA discharges with the C-wall, heating power, density, magnetic field and triangularity cover a wide range. This subset contains 930 data points. The pairwise correlations between P_{loss}, B_T and n_e are weak, but the (δ, B_T) and (δ, n_e) correlations are rather strong such that reliable regressions should not include δ. Table 6 summarises the results of the regressions.

The dependences of P_{loss}, B_T and n_e agree with those yielded by the analyses of the full database, table 4. Those of P_{loss} and B_T vary little from row to row. This in particular confirms the negative B_T and the negligible n_e dependences. The

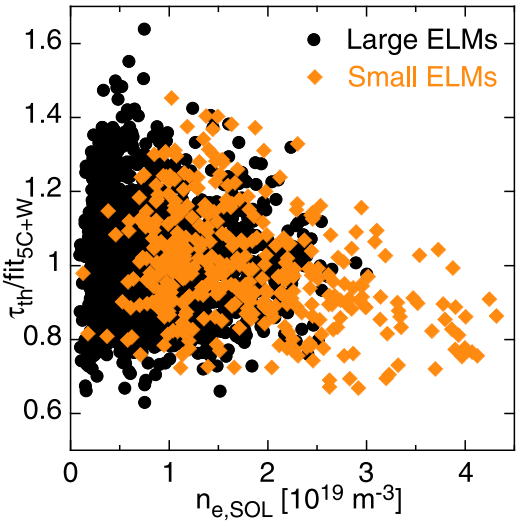

Figure 37. τ_{th} normalised by the fit_{5C+W} versus $n_{e,SOL}$ for the two ELM categories.

Table 6. Data subset for C-wall data at 1 MA in only: summary of the regressions including different regressors.

Label	ζ	α_{B_T}	α_{n_e}	$\alpha_{P_{loss}}$	RMSE
1C-1MA	0.319			−0.679	0.177
2C-1MA	0.381	−0.204		−0.687	0.176
3C-1MA	0.399	−0.222	−0.018	−0.684	0.166

1 MA data subset is sufficiently large and well conditioned such that we can go a step further and gain the dependences of τ_{th} on P_{loss}, B_T, n_e or δ separately by selecting subsets in which only one or two of these variables vary while the others are limited to a narrow range.

The results are summarised in table 7 showing that the dependences on P_{loss}, n_e and δ obtained in this way, which is almost free from correlations between regressors, yields values of the exponents in agreement with those those of tables 4 and 6 which are then confirmed. Unfortunately the 1 MA data subset does not allow us to confirm with accuracy the B_T dependence in this way.

To illustrate this approach, the heating power degradation is illustrated in figure 38 by τ_{th} plotted versus P_{loss}. This representation takes into account the two strongest dependences (I_p and P_{loss}) such that τ_{th} can indeed be used. The rather large scatter around 5 MW, which is related to a wide variation in the remaining variables, B_T, n_e and δ allows us to investigate confinement at almost constant heating power, $4.5 \leqslant P_{loss} \leqslant 5.2$ MW as done for the results reported in table 7.

Table 7. Data subset for C-wall data at 1 MA only: summary of the regressions including only one or two regressors combined with limited range for the other variables as indicated in the corresponding columns.

label	B_T (T)	δ	n_e (10^{19} m^{-3})	P_{loss} (MW)	τ_{th} dependences
1C-1MA-r	1.9–2.2	—	—	4.5–5.2	$n_e^{0.09\pm0.06}\delta^{0.26\pm0.04}$
2C-1MA-r	1.9–2.2	0.10–0.18	—	4.5–5.2	$n_e^{0.01\pm0.07}$
3C-1MA-r	1.9–2.2	0.10–0.18	—	—	$n_e^{0.01\pm0.05}P_{loss}^{-0.63\pm0.03}$
4C-1MA-r	2.3–2.7	0.22–0.28	6.0–8.0	—	$P_{loss}^{-0.66\pm0.03}$

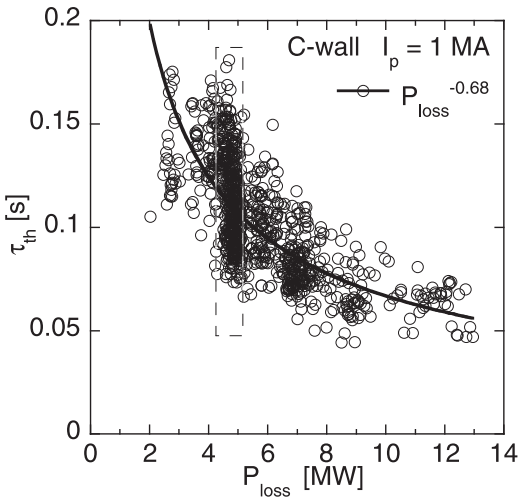

Figure 38. Data subset $I_p = 1$ MA for the C-wall. Confinement time versus heating power. The rectangle indicates the window in which the heating power is limited to for further analyses described in the text.

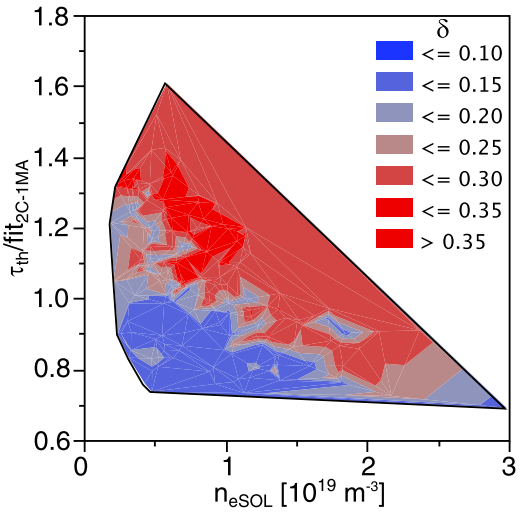

Figure 40. Data subset for the C-wall, $I_p = 1$ MA and $4.5 \leqslant P_{loss} \leqslant 5.2$ MW: plot of $\tau_{th}/\text{fit}_{2C\text{-}1MA}$ versus $n_{e,SOL}$ with contours for δ, showing that the high normalised confinement is obtained at high values of δ while $n_{e,SOL}$ is not too high.

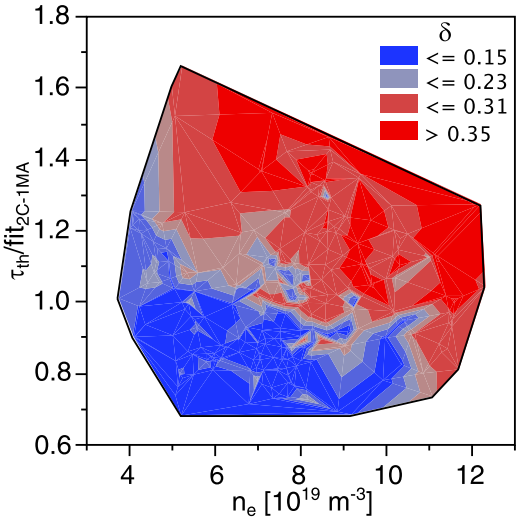

Figure 39. Data subset for the C-wall, $I_p = 1$ MA and $4.5 \leqslant P_{loss} \leqslant 5.2$ MW: plot of $\tau_{th}/\text{fit}_{2C\text{-}1MA}$ versus n_e with contours for δ, showing clearly that good normalised confinement is obtained at high values of δ.

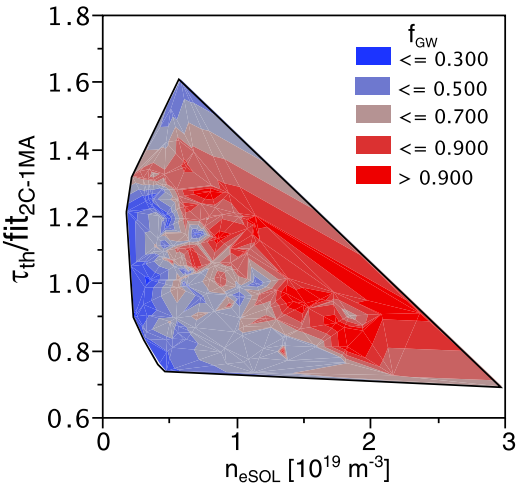

Figure 41. Data subset for the C-wall, $I_p = 1$ MA and $4.5 \leqslant P_{loss} \leqslant 5.2$ MW: plot of $\tau_{th}/\text{fit}_{2C\text{-}1MA}$ versus $n_{e,SOL}$ with contours for values of f_{GW} showing that the decrease of the upper boundary of normalised confinement with $n_{e,SOL}$ corresponds to gradually increasing values of f_{GW}.

The impact of n_e and δ can be visualised in the contour plot of figure 39 which indicates clearly that confinement is higher at higher values of δ. This plot also suggests a slight decrease of τ_{th} with density at constant triangularity which is in agreement with the results reported in [65] and with the result given in table 6.

As δ breaks the correlation between n_e and $n_{e,SOL}$ it is instructive to also investigate the dependence of τ_{th} on $n_{e,SOL}$,

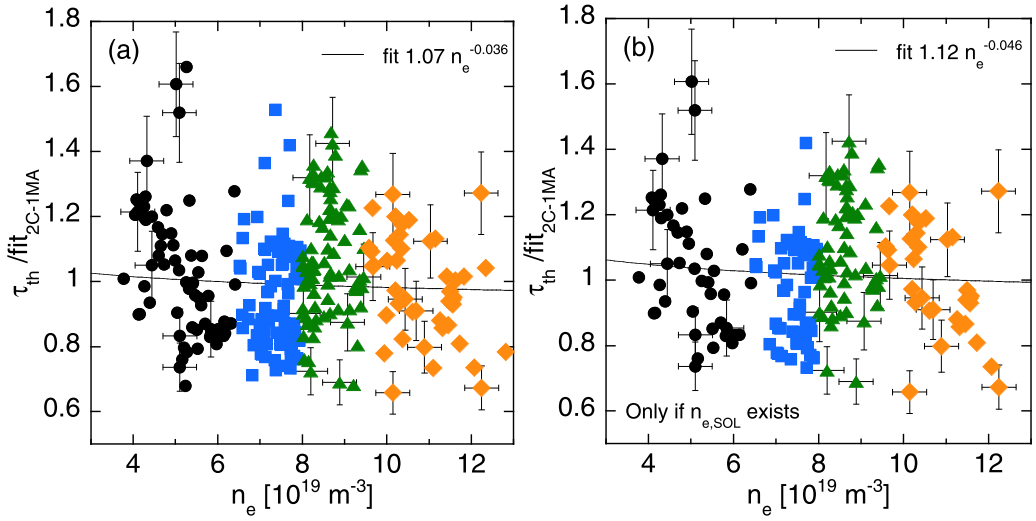

Figure 42. Data subset $I_p = 1$ MA and P_{loss} around 5 MW: confinement time versus density, panel (a) all data points, panel (b) data points for which $n_{e,SOL}$ is available. The density ranges indicated by the different symbols are used in figure 43. Only a few error bars are drawn to avoid blurring of the plots.

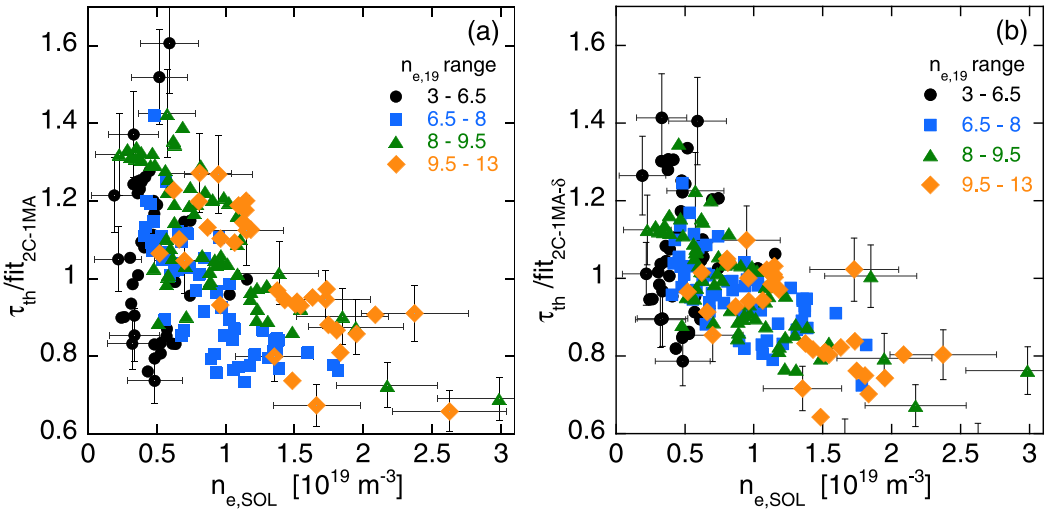

Figure 43. Data subset $I_p = 1$ MA and P_{loss} around 5 MW: dependence of τ_{th} and $\tau_{th}/\delta^{0.26}$ versus $n_{e,SOL}$.

for different values of δ. An overview is given by the contour plot figure 40. This graphic exhibits a clear triangular shape, with better confinement at higher triangularity and a very clear degradation of the higher τ_{th} values with increasing $n_{e,SOL}$, already seen in the previous section, e.g. figure 30.

The upper boundary of τ_{th} and its decrease with increasing $n_{e,SOL}$ is correlated with the proximity to the Greenwald density limit as confirmed by figure 41.

The impact of $n_{e,SOL}$ on confinement can be investigated in some more details by selecting ranges in density as indicated by the different symbols in figure 42. This figure displays $\tau_{th}/\mathrm{fit}_{2C-1MA}$ versus n_e, in panel (a) for all the data points and in panel (b) only with data points for which $n_{e,SOL}$ exists. There are therefore less points in plot (b) but the overall behaviour is unchanged showing that the analysis will not be biased by a possible lack of points in the operational space when $n_{e,SOL}$ is used. This is confirmed by the fits indicated in the two plots which both reveal a very weak negative dependence on density, also in agreement with the above results.

The effect of $n_{e,SOL}$ appears in figure 43(a) which displays $\tau_{th}/\mathrm{fit}_{2C-1MA}$ as a function of $n_{e,SOL}$ for the different density ranges indicated in figure 42. This clearly shows an overall decrease of τ_{th} with $n_{e,SOL}$ which, however, depends on the density range. In the lower density range, $n_e \leqslant 6.5 \times 10^{19}$ m^{-3}, which corresponds essentially to the natural density mainly without or with weak gas puffing, $n_{e,SOL}$ has almost no impact on τ_{th} and the large scatter remains. In contrast, a clear confinement degradation with increasing $n_{e,SOL}$ occurs for the higher density ranges for which more gas puffing is required. This orders the points rather well and induces a rather clear overlap of the data for the different n_e ranges. Thus, at low values of $n_{e,SOL}$ the variations in confinement (vertical scatter) are not due to $n_{e,SOL}$ but rather to other factors such as triangularity, electron versus ion heating or ion to electron temperature ratio.

Increasing density with gas puffing has an increasing deleterious effect on confinement related to $n_{e,SOL}$, as also reported in [60] and linked with the higher value of f_{GW} as suggested by figure 41.

The positive impact of triangularity on confinement, yielded by the regressions and illustrated by the contour plot figure 40, is clearly exhibited by figure 43(*b*) where $\tau_{th}/\mathrm{fit}_{2C-1MA}$ is in addition normalised by the $\delta^{0.26}$ dependence yielded by the analysis shown in table 7. This normalisation by δ reduces the scatter in the vertical direction for all the density ranges which improves the ordering of the points. This is particularly clear for the low density range, the lower points are shifted upwards because they have a lower triangularity. We note here that using $n_{e,SEP}$ instead of $n_{e,SOL}$ yields very similar results.

Such analyses performed at different values of plasma current and in various windows of heating power yield similar trends but are less clear because the range in n_e, $n_{e,SOL}$ and/or δ are narrower or contain a rather small amount of points. Thus the behaviour shown in the above figures is not an exception.

Summarising this section: the exponent of the confinement degradation on heating power deduced at fixed values of plasma current, where possible, lies between -0.61 and -0.68 and is therefore in agreement with the regressions made on the complete database. The positive effect of triangularity on confinement is clearly confirmed, as well as a very weak confinement degradation with increasing density at fixed value of δ. The edge density, represented here by $n_{e,SOL}$, plays also a significant role when density is increased.

7. Summary and conclusion

The contribution of the ASDEX Upgrade tokamak to the ITPA multi-machine confinement database has been presented. This dataset contains time points from H-mode discharges performed between 1994 and 2017 and therefore covers the periods of time with the C and W walls. The content of the database has been described and analyses of some features of the density and confinement time behaviour presented and discussed. This dataset probably offers possibilities to perform more detailed studies or address other topics.

The expected dependences of the density on the control plasma parameters are yielded by the database, in particular the increase with plasma current and with triangularity. Using the SOL density as approximation for the particle source indicates that, in comparison with the C-wall, a somewhat higher edge particle fuelling is required in the W-wall to reach a given Greenwald fraction. Using the separatrix density instead of the SOL density yields very similar behaviour but with a larger scatter. The Greenwald fraction is found to depend mainly on triangularity and SOL density, somewhat on magnetic field but very weakly on heating power and plasma current. Consequently, for a given value of triangularity and magnetic field, the required particle fuelling to reach a given Greenwald fraction is independent of plasma current. This is due to the almost linear increase of density with plasma current.

This dataset allows for a comparison between the confinement time in the discharges during the C-wall and W-wall periods. The very low density range is almost only populated by C data as this operational region is hampered by tungsten accumulation in discharges in the W-wall. For the medium and high density regions both C and W data are well represented. In this region of density the energy confinement time in the W-wall is about 10% lower than the C data, but the dependences are not basically different. Overall the known properties and dependences of the global confinement time are found and are in agreement with those of the analysis of the recent version of the ITPA multi-machine confinement database [3]. In particular, the stronger than linear plasma current dependence and the negative dependence on magnetic field found in the analysis of the multi-machine are confirmed. The latter is in clear contrast with the positive B_T dependence of the IPB98(y,2) scaling widely used during the last two decades. The positive impact of triangularity is also confirmed. Further, the density dependence is negligible or even slightly negative. The behaviour of the confinement time towards high density has been investigated in details in the present work. It confirms previous results which suggested that towards high Greenwald fraction values the density profile in the plasma edge, including separatrix and SOL, causes a confinement degradation. This is attributed to the reduction of the pedestal stability induced by an outwards shift of the pedestal density profile, as demonstrated in pedestal studies. This is consistent with the fact that the confinement time in the W-wall is about 10% lower than with the C-wall because the somewhat higher edge particle fuelling required with the W-wall increases the outwards shift of the pedestal density profile. The fact that high triangularity provides high core density for low SOL density, corresponding to lower edge fuelling, contributes to the enhancement of the confinement with triangularity.

The AUG present database is rather well conditioned for confinement studies but some improvements might be possible through data mining of existing discharges or new dedicated discharges to improve in particular the W-wall dataset of the database. One of the useful extensions would be to include, if they exist, data at lower density for the W-wall, in particular at 1 MA to reduce the correlation between I_p and n_e. Experiments in this direction have been carried out recently. Data from recent dedicated B_T scans in the W-wall [72] should also improve the database condition and hopefully provide a more accurate assessment of the B_T dependence. Further, data at lower triangularity for the W-wall would also contribute to better assess the dependences of the W dataset.

Considering the results presented here on the relation between SOL density and density on one hand and its effect on confinement time through the pedestal stability on the other hand, a multi-machine study seems desirable to address these topics in comparisons between several devices.

Acknowledgments

This work has been partly carried out within the framework of the EUROfusion Consortium and has received funding from the Euratom research and training programme 2014–2018 and 2019–2020 under Grant Agreement Number 633053. The

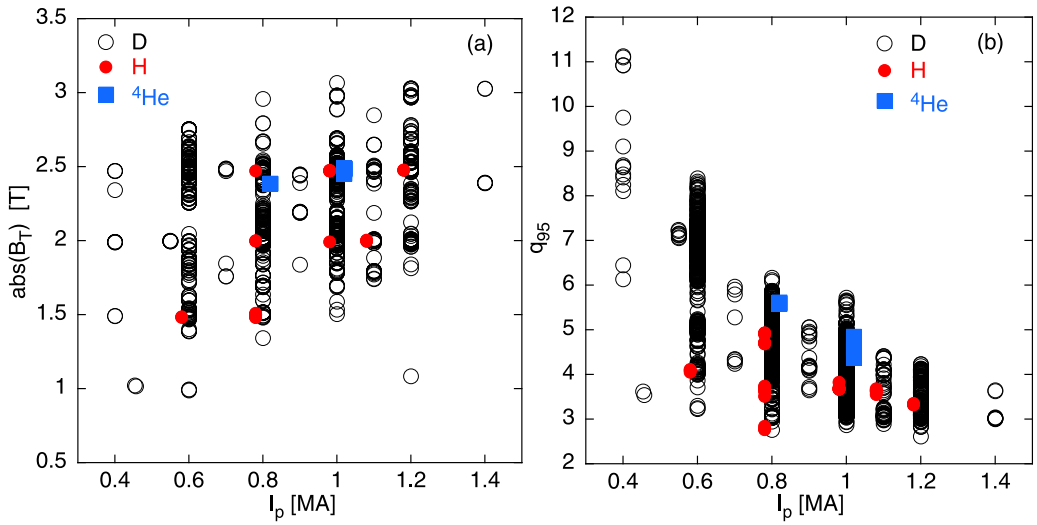

Figure 44. (*a*) Magnetic field versus plasma current showing the repartition of the hydrogen and helium points in comparison to deuterium. (*b*) Edge safety factor versus plasma current. The different working gases are indicated by the different symbols.

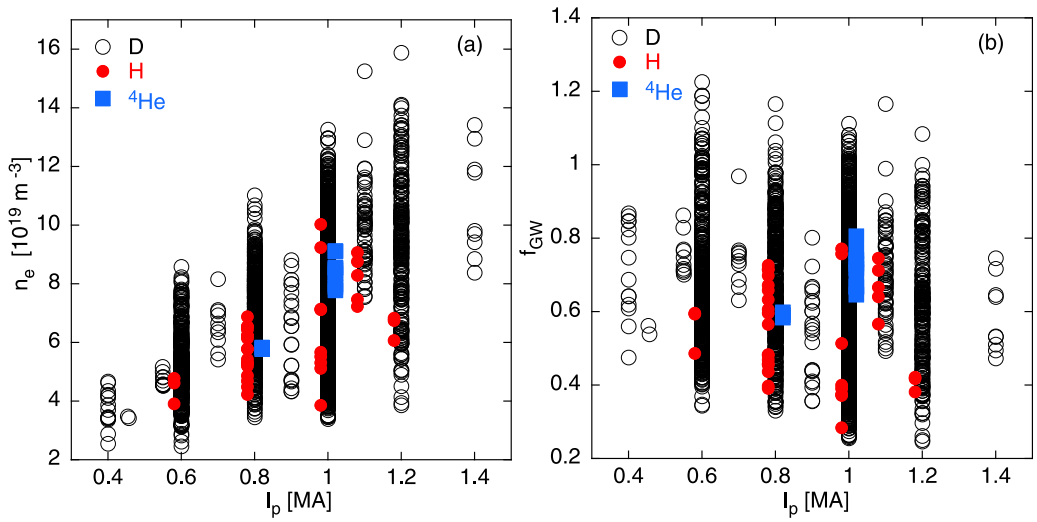

Figure 45. Electron density versus plasma current showing the repartition for the three gases: panel (*a*) line average density; panel (*b*) Greenwald fraction. The different working gases are indicated by the different symbols.

views and opinions expressed herein do not necessarily reflect those of the European Commission.

Appendix A. Working gas

The main working gas in AUG is deuterium (D) but discharges in hydrogen (H) and in helium (He^4) have also been run and some of them are included in the present database: 38 time points in H and 17 in He^4. The hydrogen discharges can be heated with H-NBI, ECRH and/or ICRH which provides pure hydrogen plasmas. The maximum heating power available for H-NBI is 13 MW is therefore significantly lower than that of D-NBI. For helium plasmas, NBI can be either H or D but not helium because operating the NBI system with this gas does not deliver enough power for a sufficiently long duration to provide valuable experimental results [85]. Therefore the helium discharges are hampered by this lack of gas purity, except if ECRH and/or ICRH only are used.

The hydrogen discharges made throughout the years were designed to be, despite their small number, rather well distributed over the range of the various control parameters. These data points are included in the mass dependence deduced from the ITPA database [3]. In contrast, the helium discharges are limited in to a few values in operational space and are only provided for comparisons. More information on the study of the isotope effect (H and D) in AUG can be found in [39, 40] and for helium in [86, 87].

The repartition of the H and He points in the database are shown in the following figures. Figure 44(*a*) shows the ranges of plasma current and magnetic field. In this plot we also indicate the working gas deuterium (D), hydrogen (H) and helium (He^4). For more clarity, the I_p values in MA have been rounded such that the second decimal is 0 or 5 for the deuterium points,

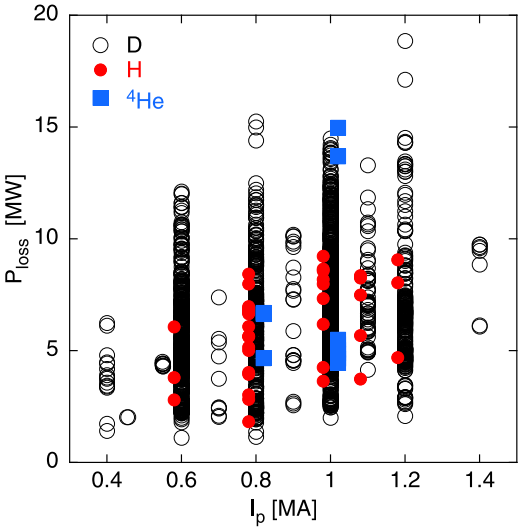

Figure 46. Loss power versus plasma current showing the repartition for the three gases.

Table 8. List of number of time points with different impurity seeding species.

Impurity	He	N_2	Ne	Ar
No. of points	172	78	61	4

while for the hydrogen and helium points the I_p value has been in addition shifted by ± 0.02. Correspondingly the range in q_{95} for the three gases is shown in figure 44(*b*). Figures 45(*a*) and (*b*) provide the ranges in density and Greenwald fraction respectively. These figures indicate that the data in hydrogen are indeed rather well distributed over I_p, q_{95} and f_{GW}.

The repartition of the loss power is also shown in figure 46. For most of the I_p values this quantity is well distributed but remains below 10 MW, which is mainly due to the lower NBI power available for hydrogen beams. Only about ten discharges with H-NBI higher than 10 MW have been performed very recently, years 2019 and 2020. Data from these discharges could be added to a future version of the database.

A.1. Impurity seeding

Some points from discharges with impurity seeding have been included in the database. The different impurities and the number of time points are listed in table 8.

The gas nature of the seeded impurity is included in the database but the values of the impurity concentration are not available in the database. Helium has been introduced originally to investigate helium transport and pumping [29], a crucial issue for ITER. In the past the AUG vessel has often been conditioned with ^{4}He glow discharge, a residual concentration up to 10% was always intrinsically present in the plasmas, leading to poorer confinement, as reported in [30]. Such glow discharges have been avoided as much as possible after this effect had been discovered.

The other impurities have been mainly used to increase the radiation losses, particularly at the edge and in the divertor to reduce the divertor load, see e.g. [32, 33]. In particular, nitrogen has been extensively used during the recent years, whereby it has been found that N-seeding induces a confinement improvement through its impact on the pedestal density profile [36, 37]. The reader is referred to these publications for more details on the possible effect on confinement.

ORCID iDs

C. Angioni https://orcid.org/0000-0003-0270-9630
P. David https://orcid.org/0000-0003-4837-8507
T. Pütterich https://orcid.org/0000-0002-8487-4973
J. Stober https://orcid.org/0000-0002-5150-9224

References

[1] ITER Physics Expert Groups on Confinement and Transport and Confinement Modelling and Database and ITER Physics Basis Editors 1999 *Nucl. Fusion* **39** 2175–208
[2] McDonald D.C. *et al* 2007 *Nucl. Fusion* **47** 147
[3] Verdoolaege G. *et al* 2021 *Nucl. Fusion* submitted
[4] Maslov M., Boboc A., Brix M., Flanagan J.C., Peluso E., Price C. and Romanelli M. 2020 *Nucl. Fusion* **60** 036007
[5] McDonald D.C. *et al* 2008 *Plasma Phys. Control. Fusion* **50** 124013
[6] Neu R. *et al* 2007 *J. Nucl. Mater.* **363–365** 52
[7] Neu R. *et al* 2007 *J. Nucl. Mater.* **367–370** 1497
[8] Sips A.C.C. and Gruber O. 2008 *Plasma Phys. Control. Fusion* **50** 124028
[9] Neu R. *et al* 2013 *J. Nucl. Mater.* **438** S34
[10] Ryter F. *et al* 2013 *Nucl. Fusion* **53** 113003
[11] Shao L.M. *et al* 2016 *Plasma Phys. Control. Fusion* **58** 025004
[12] Lunt T., Reimold F., Wolfrum E., Carralero D., Feng Y. and Schmid K. 2017 *Plasma Phys. Control. Fusion* **59** 055016
[13] Streibl B., Lang P.T., Leuterer F., Noterdaeme J.-M. and Stäbler A. 2003 *Fusion Sci. Technol.* **44** 578
[14] Stäbler A., Hobirk J., Leuterer F., Meo F. and Noterdaeme J.-M. 2003 *Fusion Sci. Technol.* **44** 730
[15] Leuterer F. *et al* 2001 *Fusion Eng. Des.* **56–57** 615
[16] Leuterer F. *et al* 2005 *Fusion Eng. Des.* **74** 199
[17] Leuterer F. *et al* 2009 *Fusion Sci. Technol.* **55** 31
[18] Neuhauser J., Bosch H.-S., Coster D., Herrmann A. and Kallenbach A. 2003 *Fusion Sci. Technol.* **44** 659
[19] Herrmann A., Jaksic N., Leitenstern P., Greuner H., Krieger K., de Marné P., Oberkofler M., Rohde V. and Schall G. 2015 *Fusion Eng. Des.* **98–99** 1496
[20] Herrmann A., Zammuto I., Balden M., Greuner H., Jaksic N., Kallenbach A., Li M., Neu R. and Rohde V. 2017 *Nucl. Mater. Energy* **12** 205
[21] Tardini G. *et al* 2021 *Nucl. Fusion* **61** 36030 submitted
[22] Weiland M., Bilato R., Dux R., Geiger B., Lebschy A., Felici F., Fischer R., Rittich D. and van Zeeland M. 2018 *Nucl. Fusion* **58** 082032
[23] Thomsen K. *et al* 1994 *Nucl. Fusion* **34** 131
[24] Neu R. *et al* 2011 *Plasma Phys. Control. Fusion* **53** 124040
[25] Kallenbach A. *et al* 1999 *Plasma Phys. Control. Fusion* **41** B177
[26] Ryter F. *et al* 2001 *Nucl. Fusion* **41** 537
[27] Willensdorfer M. *et al* 2014 *Plasma Phys. Control. Fusion* **56** 025008
[28] Haas G. and Bosch H.-S. 1998 *Vacuum* **51** 39
[29] Bosch H.-S., Ullrich W., Bard A., Coster D., Haas G., Kallenbach A., Neuhauser J., Schneider R. and Upgrade Team A. 1999 *J. Nucl. Mater.* **266–269** 462
[30] Neu R. *et al* 2008 Europhysics conference abstracts *CD-ROM Proc. 35th EPS Conf. on Plasma Physics* (Hersonissos, Crete 2008 vol 32D ed P. Lalousis *et al* (Geneva:

EPS) http://epsppd.epfl.ch/Hersonissos/pdf/P4_039.pdf p 4.039
[31] Kappatou A. *et al* 2020 *Proc. 27th IAEA Fusion Energy Conf.* (Ahmedabad, India 2020) vol IAEA-CN–258 (Vienna: IAEA) (https://conferences.iaea.org/event/151/contributions/6454/) p EX/P8-1
[32] Kallenbach A. *et al* 2013 *Plasma Phys. Control. Fusion* **55** 124041
[33] Kallenbach A., Sun H.J., Eich T., Carralero D., Hobirk J., Scarabosio A. and Siccinio M. 2018 *Plasma Phys. Control. Fusion* **60** 045006
[34] Schweinzer J. *et al* 2011 *Nucl. Fusion* **51** 113003
[35] Tardini G. *et al* 2013 *Plasma Phys. Control. Fusion* **55** 015010
[36] Dunne M.G. *et al* 2017 *Plasma Phys. Control. Fusion* **59** 014017
[37] Dunne M.G. *et al* 2017 *Plasma Phys. Control. Fusion* **59** 025010
[38] Frassinetti L. *et al* 2019 *Nucl. Fusion* **59** 076038
[39] Schneider P. *et al* 2017 *Nucl. Fusion* **57** 066003
[40] Schneider P. A. 2021 *Nucl. Fusion* **61** 36033
[41] Neu R. *et al* 2002 *Plasma Phys. Control. Fusion* **44** 811
[42] Neu R. *et al* 2005 *Nucl. Fusion* **45** 209
[43] Angioni C., Bilato R., Casson F.J., Fable E., Mantica P., Odstrcil T. and Valisa M. 2017 *Nucl. Fusion* **57** 022009
[44] Angioni C., Sertoli M., Bilato R., Bobkov V., Loarte A., Ochoukov R., Odstrcil T., Pütterich T. and Stober J. 2017 *Nucl. Fusion* **57** 056015
[45] Gruber O. *et al* 1995 *Phys. Rev. Lett.* **74** 4217
[46] Kallenbach A. *et al* 1996 *Plasma Phys. Control. Fusion* **38** 2097
[47] Gruber O. *et al* 2000 *Plasma Phys. Control. Fusion* **42** A117
[48] Wolf R.C. *et al* 2001 *Nucl. Fusion* **41** 1259
[49] Stober J. *et al* 2007 *Nucl. Fusion* **47** 728
[50] Manini A. *et al* 2004 *Plasma Phys. Control. Fusion* **46** 1723
[51] Manini A., Angioni C., Peeters A.G., Ryter F., Jacchia A., Maggi C.F. and Suttrop W. 2006 *Nucl. Fusion* **46** 1047
[52] Stober J. *et al* 2015 *EPJ Web Conf.* **87** 02004
[53] Stober J. *et al* 2016 *Proc. 26th IAEA Fusion Energy Conf.* (Kyoto, Japan 2016 vol IAEA-CN-234 (Vienna: IAEA) (https://nucleus.iaea.org/sites/fusionportal/Shared%20Documents/FEC%202016/fec2016-preprints/preprint0799.pdf) p DP 4
[54] Bock A. *et al* 2018 *Phys. Plasmas* **25** 056115
[55] Schweinzer J. *et al* 2016 *Nucl. Fusion* **56** 106007
[56] Neu R. *et al* 2016 *IEEE Trans. Plasma Sci.* **44** 1472
[57] Sips A. *et al* 2018 *Nucl. Fusion* **58** 126010
[58] Bosch H.-S. *et al* 1999 *Plasma Phys. Control. Fusion* **41** A401
[59] Carralero D. *et al* 2014 *Nucl. Fusion* **54** 123005
[60] Bernert M. *et al* 2015 *Plasma Phys. Control. Fusion* **57** 014038
[61] Eich T., Goldston R.J., Kallenbach A., Sieglin B. and Sun H.J. 2018 *Nucl. Fusion* **58** 034001
[62] Suttrop W., Gehre O., Fuchs J.C., Reimerdes H., Schneider W. and Schweinzer J. 1998 *Plasma Phys. Control. Fusion* **40** 771
[63] Angioni C., Peeters A.G., Pereverzev G.V., Bottino A., Candy J., Dux R., Fable E., Hein T. and Waltz R.E. 2009 *Nucl. Fusion* **49** 055013
[64] Reimold F., Wischmeier M., Bernert M., Potzel S., Kallenbach A., Müller H.W., Sieglin B. and Stroth U. 2015 *Nucl. Fusion* **55** 033004
[65] Stober J., Gruber O., Kallenbach A., Mertens V., Ryter F., Stäbler A., Suttrop W. and Treutterer W. 2000 *Plasma Phys. Control. Fusion* **42** A211
[66] Saibene G. *et al* 2002 *Plasma Phys. Control. Fusion* **44** 1769
[67] Luda T., Angioni C., Dunne M.G., Fable E., Kallenbach A., Bonanomi N., Schneider P.A., Siccinio M. and Tardini G. 2020 *Nucl. Fusion* **60** 036023
[68] Wagner F. *et al* 1991 Plasma physics and controlled fusion research *Proc. 13th Int. Conf.* (Washington 1990) vol 1 (Vienna: IAEA) p 277
[69] Ryter F., Fahrbach H.-U., Gude A., Neu R., Rohde V. and Stober J. 2002 *Plasma Phys. Control. Fusion* **44** A407
[70] https://jmp.com/en-in/statistics-knowledge-portal/what-is-correlation/correlation-coefficient.html
[71] Cordey J.G. 2003 *Nucl. Fusion* **43** 670
[72] Luda T. private communication
[73] Romanelli F. *et al* 1989 *Plasma Phys. Control. Fusion* **31** 1535
[74] Guo S.C. and Romanelli F. 1993 *Phys. Fluids*B **5** 520
[75] Ryter F. *et al* 2019 *Nucl. Fusion* **59** 096052
[76] Viezzer E. 2018 *Nucl. Fusion* **58** 115002
[77] Harrer G.F. *et al* 2018 *Nucl. Fusion* **58** 112001
[78] Zohm H. 1996 *Plasma Phys. Control. Fusion* **38** 105
[79] Stober J., Fuchs C., Gruber O., Kaufmann M., Kurzan B., Meo F., Müller H.W. and Ryter F. 2001 *Nucl. Fusion* **41** 1535
[80] Stober J. *et al* 2005 *Nucl. Fusion* **45** 1213
[81] Boom J.E. *et al* 2012 *Nucl. Fusion* **52** 114004
[82] Wolfrum E. *et al* 2011 *Plasma Phys. Control. Fusion* **53** 085026
[83] Martin Y.R. and Takizuka T. 2008 *J. Phys.: Conf. Ser.* **123** 012033
[84] Ryter F., Fuchs J., Schneider W., Sips A., Stäbler A. and Stober J. 2008 *J. Phys.: Conf. Ser.* **123** 012035
[85] Hopf C., Rittich D., Schäffler J. and Thalhammer J. 2017 *Fusion Eng. Des.* **123** 281
[86] Ryter F. *et al* 2009 *Nucl. Fusion* **49** 062003
[87] Manas P., Angioni C., Kappatou A., Ryter F. and Schneider P.A. 2019 *Nucl. Fusion* **59** 014002